

Source and Pathway of the Western Arctic Upper Halocline in a Data-Constrained Coupled Ocean and Sea Ice Model

AN T. NGUYEN

Massachusetts Institute of Technology, Cambridge, Massachusetts

RONALD KWOK AND DIMITRIS MENEMENLIS

Jet Propulsion Laboratory, California Institute of Technology, Pasadena, California

(Manuscript received 23 February 2011, in final form 27 November 2011)

ABSTRACT

A coupled ocean and sea ice model is used to investigate dense water (DW) formation in the Chukchi and Bering shelves and the pathways by which this water feeds the upper halocline. Two 1992–2008 data-constrained solutions at 9- and 4-km horizontal grid spacing show that 1) winter sea ice growth results in brine rejection and DW formation; 2) the DW flows primarily down Barrow and Central–Herald Canyons in the form of bottom-trapped, intermittent currents to depths of 50–150 m from the late winter to late summer seasons; and 3) eddies with diameters ~ 30 km carry the cold DW from the shelf break into the Canada Basin interior at depths of 50–150 m. The 4-km data-constrained solution does not show eddy transport across the Chukchi Shelf at shallow depths; instead, advection of DW downstream of polynya regions is driven by a strong (~ 0.1 m s⁻¹) mean current on the Chukchi Shelf. Upper halocline water (UHW) formation rate was obtained from two methods: one is based on satellite data and on a simple parameterized approach, and the other is computed from the authors' model solution. The two methods yield 5740 ± 1420 km³ yr⁻¹ and 4190 – 4860 ± 1440 km³ yr⁻¹, respectively. These rates imply a halocline replenishment period of 10–21 yr. Passive tracers also show that water with highest density forms in the Gulf of Anadyr and along the eastern Siberian coast immediately north of the Bering Strait. These results provide a coherent picture of the seasonal development of UHW at high spatial and temporal resolutions and serve as a guide for improving understanding of water-mass formation in the western Arctic Ocean.

1. Introduction

The Arctic Ocean halocline, a layer of high vertical salinity gradient and of near-freezing temperature, insulates the surface sea ice from heat stored in Atlantic Water and has a significant impact on sea ice growth and melt (Aagaard et al. 1981; Steele and Boyd 1998; Rudels et al. 2004). Despite its importance, our understanding of Arctic halocline ventilation remains limited because of a lack of direct observations. In the literature, the halocline is often divided into an upper and lower layer based on the distinctive temperature and salinity (T – S) properties and origins of each layer. Figure 1 summarizes the qualitative definitions of Arctic upper halocline

water (UHW) and lower halocline water (LHW) and the various mechanisms for halocline ventilation proposed by Weingartner et al. (1998), Woodgate et al. (2005a), Shimada et al. (2005), Pickart (2004), and Pickart et al. (2005). Ranges of salinity are approximately 32–33.3 psu for UHW and 33.3–34.3 psu for LHW. For studies of water-mass formation, Pickart (2004) and Woodgate et al. (2005a) also define core salinities for the UHW and LHW as approximately 32.85–33.1 and 34.0 psu, respectively.

The source and pathways of both the LHW and UHW are subjects of ongoing investigations. In this paper, we focus on the formation and ventilation of the UHW. For completeness, we first review current understanding of mechanisms for LHW and UHW ventilation and how they are related. Because of its higher salinity, the LHW is thought to be of Atlantic origin (Steele and Boyd 1998; Rudels et al. 2004). Woodgate et al. (2005a), however, showed that diapycnal mixing between Atlantic and

Corresponding author address: An T. Nguyen, Massachusetts Institute of Technology, 54-1410, 77 Massachusetts Ave., Cambridge, MA 02139.
E-mail: atnguyen@mit.edu

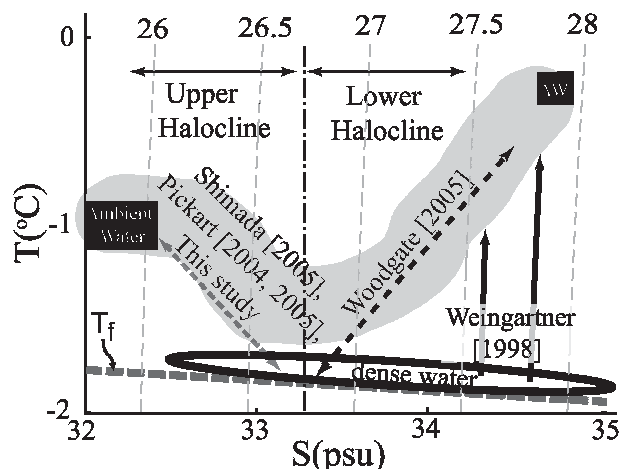


FIG. 1. The T - S characteristic of the halocline in the western Arctic Ocean (light gray area). Salinities are 32.85–33.1 psu for the UHW and 33.1–34 psu for the LHW. The separation between these two water masses ranges from 33.2 to 33.5 psu (vertical dashed-dotted line). DW in this study is defined as a combined hypersaline ($T < -1.6^{\circ}\text{C}$ and $S > 34$ psu) and Pacific winter-transformed ($T < -1.4^{\circ}\text{C}$ and $32.5 \text{ psu} \# S \# 33.6$ psu) water. See section 1 for discussion on the various halocline formation mechanisms suggested by Weingartner et al. (1998), Woodgate et al. (2005a), Shimada et al. (2005), Pickart (2004), Pickart et al. (2005), and this study. The two vertical black arrows imply that the hypersaline water can ventilate the lower halocline directly in salinity space by the mechanism of gravity-driven flow downslope to neutral buoyancy depth Weingartner et al. (1998). The freezing temperature T_f line is also shown for reference.

Pacific Winter Water could be a potential mechanism for ventilation of the LHW. Weingartner et al. (1998) suggested that water formed during polynya events, which he referred to as hypersaline water with near-freezing temperature and salinity $S > 34$ psu, could also be a source of LHW (black open oval in Fig. 1). As for the UHW, oxygen data analysis by Shimada et al. (2005) suggests that hypersaline water of Pacific origin ventilates the upper part of the halocline in the southern Canada Basin in the vicinity of the Alaskan coast. In addition to chemical tracers, Pickart (2004) and Pickart et al. (2005) also used hydrographic profiles to show that winter-transformed Bering Water ($T < -1.4^{\circ}\text{C}$ and $32.5 \text{ psu} \# S \# 33.6$ psu), which flows off the Chukchi Shelf via Barrow Canyon (BC) and Herald Canyon (HC), ventilates the upper halocline.

In addition to these observations, theoretical and numerical studies have been conducted by Gawarkiewicz and Chapman (1995, hereafter GC95), Chapman and Gawarkiewicz (1995, hereafter CG95), and Gawarkiewicz (2000) to specifically examine dense water (DW) formation and pathways on an idealized shelf. Dense water here refers to the combination of hypersaline and winter-transformed Pacific Water. These studies suggest that shelf

eddies, which form because of frontal instability associated with coastal and bottom friction, serve as the main agent for transport of the DW to the shelf break. These eddies have characteristic length scales of ~ 15 km, time scales of growth of 6–10 days, and velocity magnitudes of 0.01 – 0.02 m s^{-1} ; these scales implies a cross-shelf transit time scale of 10–30 days. This eddy transport mechanism limits the maximum shelf density anomaly within the DW to 0.2 – 1.0 kg m^{-3} (GC95). When a submarine canyon such as Barrow or Herald Canyon is present, DW tends to collect inside the canyons and is carried off shelf episodically both as gravity-driven plumes and as eddy-driven slumps (CG95; Chapman 2000). The time scale of transports down the canyon from the canyon's mouth is ~ 14 days. In the Canada Basin interior, the depth to which this DW reaches is determined by the location of the DW source and by the vertical stratification of the water column seaward of the shelf break (Gawarkiewicz 2000). In the case of the Chukchi Shelf, where a high-density (salinity) gradient exists (i.e., the halocline), the bottom-trapped DW is first carried by eddies to the shelf break at typical velocity of $\sim 0.05 \text{ m s}^{-1}$; it then flows as frictional gravity current down to depths of 90–165 m (Gawarkiewicz 2000). The time scale of eddy transport from the source to depths of 90–165 m in the halocline is ~ 90 days.

The fate of the DW at the shelf break, at depths of 50–150 m, is investigated by Spall et al. (2008) using an idealized 1-km primitive equation model. They found that the DW is carried into the Canada Basin interior by dominantly cold-core anticyclonic eddies. These eddies, different from those formed on the shelf, develop along the Chukchi Shelf edge at middepth and have diameters of 20–30 km.

Related to the DW transport mechanisms both on the Chukchi Shelf and in the basin interior is the question of how much of the Pacific DW contributes to UHW in term of production rates. Cavalieri and Martin (1994, hereafter CM94) provided a first regional estimate of UHW production in the western Arctic Ocean for the period 1978–87 using satellite-derived sea ice concentration, in situ measurements of sea surface salinity, and basic assumptions about properties of halocline water. UHW in CM94 is defined as the resultant water mass of the mixing between DW and ambient lighter water (Fig. 1). A key assumption here is that all of the DW flows off the Chukchi Shelf into the Arctic Ocean interior and replenishes the halocline. Even though this assumption is partially supported by observations of off-shelf flows from hydrographic profiles (Melling 1993; Pickart 2004; Pickart et al. 2005), numerical studies have shown that such assumptions can be erroneous (Winsor and Björk 2000; Gawarkiewicz 2000). In particular,

Gawarkiewicz (2000) showed that only approximately half of the DW from the source reaches the halocline depth to become UHW, whereas the rest remains on the shelf or is transported off shelf to shallow depths, which then mixes with ambient water. It is important to note that numerical UHW production estimates, in general, can be highly sensitive to the atmospheric forcing used in the model. As an example, Winsor and Chapman (2002) showed that a high-resolution meteorological forcing on the Chukchi Shelf yields dense shelf water with typical salinity anomalies of 1.5 psu instead of the 1.0-psu salinity anomaly obtained using the National Centers for Environmental Prediction (NCEP) reanalysis. This difference in maximum salinity anomaly on the shelf can result in ~20% difference in the production rates of DW that ventilates the halocline (see, e.g., Fig. 7 of Winsor and Chapman 2002).

The nomenclature we adopt in the rest of this study is as follows: DW is defined as the combined hypersaline water ($S > 33.6$ psu and $T < -1.8^{\circ}\text{C}$; Weingartner et al. 1998) and winter-transformed Pacific Water ($32.3 \leq S \leq 33.6$ psu and $T < -1.3^{\circ}\text{C}$; Pickart et al. 2005) that form on the shelf. UHW is defined in two ways depending on the context. When pertaining to the CM94 method, UHW is the resultant product of the mixing between two end members: dense and ambient (lighter) water masses (Fig. 1). For the numerical model analyses, UHW is the portion of DW that crosses the 50-m isobath at the shelf slope and penetrates down to greater depths.

Two data-constrained coupled ocean and sea ice simulations at 9- and 4-km horizontal grid spacing are used in this study to investigate the main mechanism for ventilating the UHW. Specifically, we calculate production rates of DW on the Chukchi Shelf and trace this water as it flows off the shelf slope into the Canada Basin. The primary motivation for using solutions at 9- and 4-km grid spacing is to investigate the dependence of horizontal resolution on DW production and more importantly on the transport of this DW both on the Chukchi Shelf and in the Canada Basin interior. Because most global models currently cannot achieve horizontal grid spacing beyond 9-km, this study can potentially offer an assessment of the capability of global and pan-Arctic coupled ocean and sea ice models to simulate DW production and upper halocline ventilation. The use of the eddy-permitting 4-km solution allows us to investigate the contribution of eddy transport of DW into the halocline.

We estimate UHW production using two approaches: one follows CM94 and the other uses the model T - S output and passive tracers. A comparison of the two methods will enable us to assess the validity of the various CM94 assumptions. When applicable, we compare

our results of DW and UHW production rates and pathways with those from existing studies. The paper is organized as follows: Section 2 describes the model and the calculations of sea ice, DW, UHW production rates, and eddy transports. Results and discussions of sea ice, DW, UHW production, and eddy transports are in section 3. Summary and concluding remarks follow in section 4.

2. Method

In this section, we first describe the model and the study area and then describe the methods for calculating productions of sea ice, DW, UHW, and eddy transports.

a. Model description

This study is based on a regional Arctic configuration of the Massachusetts Institute of Technology general circulation model (MITgcm) (Marshall et al. 1997a,b). The ocean model is coupled to a dynamic/thermodynamic sea ice model, as described in Menemenlis et al. (2005b), Losch et al. (2010), and Heimbach et al. (2010). The model configuration is identical to that of Nguyen et al. (2011), with the exception that the horizontal grid spacing has been decreased from 18 km to 9 and 4 km and the bathymetry has been updated accordingly in order to better resolve the flow down the narrow and steep Barrow Canyon. Bathymetry for the 9-km solution is from the blend S2004 (Marks and Smith 2006) with minor modifications in the Barrow Canyon to ensure that the canyon slopes match with those from Pickart et al. (2005). For the 4-km solution, we merged S2004 with the International Bathymetric Chart of the Arctic Ocean (IBCAO; Jakobsson et al. 2008). No special treatment for Barrow Canyon was employed in the merged bathymetry.

Salt rejected during sea ice formation is treated using the subgrid-scale salt plume parameterization of Nguyen et al. (2009). This parameterization is key to permitting a realistic representation of the upper halocline in the 18-km solution of Nguyen et al. (2011). Model parameters, initial conditions, and surface boundary conditions for the 18-km solution were selected and adjusted using the Green's function approach of Menemenlis et al. (2005a) to fit a large complement of hydrographic and sea ice observations (see Table 2 of Nguyen et al. 2011). Monthly-mean estuarine fluxes of freshwater are based on the Regional, Electronic, Hydrographic Data Network for the Arctic Region (R-ArcticNET) dataset (Lammers et al. 2001).

As in Nguyen et al. (2011), sea ice initial conditions for January 1992 are from the Polar Science Center (Zhang and Rothrock 2003) and ocean initial conditions are from the *World Ocean Atlas 2005* (Antonov et al. 2006; Locarnini et al. 2006). Surface boundary conditions are

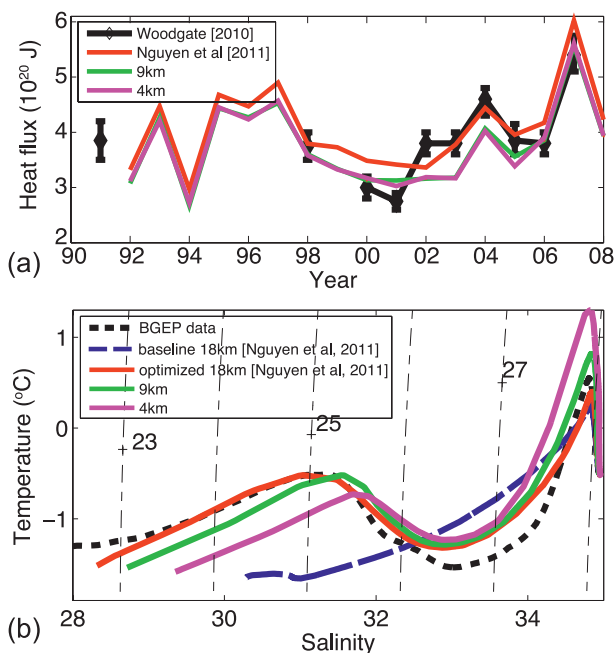


FIG. 2. (a) Annual heat transport comparison between model solutions and observations from Woodgate et al. (2010) and (b) T - S properties of water masses in the Canada Basin from model solutions and Beaufort Gyre Exploration Project (BGEF) data for August 2003. In (a), the difference in the 17-yr-mean heat transports is 8% between Nguyen et al. (2011) optimized solution and those in the 9- and 4-km solutions. In (b), the halocline between potential density σ of 25–27 kg m^{-3} (contour lines) are present in both the 9- and 4-km solutions.

from the Japanese 25-year Reanalysis (JRA25; Onogi et al. 2007). Lateral boundary conditions are from the partially constrained Estimating the Circulation and Climate of the Ocean, Phase II (ECCO2) solution (Menemenlis et al. 2008). No surface temperature and salinity restoring is used. The integration period is 1992–2008. We did not see any large model drift at the beginning of the integration period. As a precaution, however, analyses shown in this study begin in January 1995. Several subsequent time series of heat flux across Bering Strait, sea ice production, and DW production will be shown here to address the stability of the solutions.

To assess the 9- and 4-km solutions, we calculated the model–data misfits and compared with those from the optimized 18-km solution in Nguyen et al. (2011). The most relevant assessments are transports across Bering Strait and the hydrography in the western Arctic Ocean (Fig. 2). The largest difference between the solutions is the drift in the core temperature of the Atlantic Water layer in the model, which is enhanced as horizontal resolution increases (Fig. 2b). There is also a small change in the net heat and volume (8%) transports across Bering Strait. The increase of misfits in the higher-resolution

solutions is expected because the 18-km optimized parameters for ocean mixing and transports are resolution dependent and because the 9- and 4-km solutions have higher eddy activity. We discuss any effect of these differences on DW production in section 3. The overall properties of water masses above 150 m in both the 9- and 4-km solutions, however, are consistent with those in the optimized solution that was assessed in Nguyen et al. (2011). We note that additional assessments of these three solutions can be found in Holloway et al. (2011).

Figure 3 shows the regional Arctic Ocean model domain and an inset of the study area, which includes the Chukchi and Bering Seas. Water flows from Bering Strait into the Arctic Ocean interior through four main pathways: Barrow Canyon, Central Channel (CC), Herald Canyon, and Long Strait (Fig. 3; Woodgate et al. 2005b; Pickart et al. 2005). Of these pathways, BC is the steepest, which induces the most energetic downslope flow (Pickart et al. 2005). As we will show using passive tracers, there is negligible flow down Long Strait. Thus, gates BC and CC + HC, as shown in Fig. 3, are sufficient to capture dense shelf water flux down the slopes. Note that gate CC + HC covers both CC and HC as well as the shelf slope connecting the two canyons.

b. Calculations following CM94

This section describes the steps to obtain sea ice, DW, and UHW production rates using CM94 procedure. The five key assumptions CM94 made are 1) the starting date of winter, 2) the sea surface salinity, 3) the enhanced salinity of DW, 4) the core UHW salinity, and 5) that all DW makes its way to the halocline. As we try to reproduce CM94's calculations, we made similar assumptions but further discuss how we test sensitivities of our results to such assumptions. The purpose of this exercise is to gain understanding into the effect of various assumptions and to compare production rates with our numerical results. Only the 9-km solution is used in this section.

1) SEA ICE PRODUCTION CALCULATIONS

CM94 assumed an early and a late start date to define the beginning of winter (assumption 1), then used open water fraction from the *Nimbus-7* Scanning Multichannel Microwave Radiometer (SMMR) and meteorological data to estimate net heat loss during each winter. We follow the CM94 procedure using open water fraction from the Special Sensor Microwave Imager (SSM/I) and atmospheric boundary conditions from JRA25 to calculate heat loss. These results are also compared with the model output of heat loss for evaluation purpose. These early and late start dates correspond to the time when their regions have 15% and 80% sea ice, respectively.

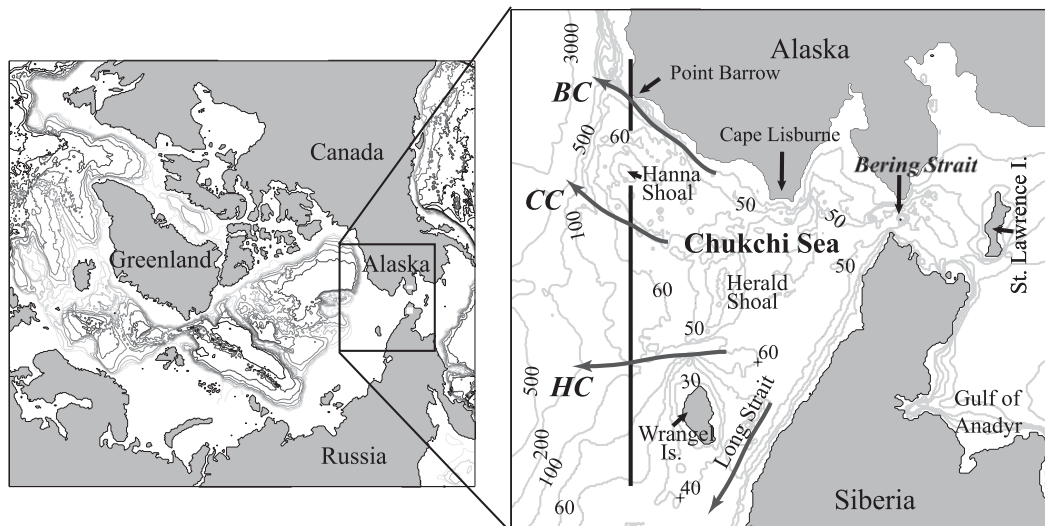


FIG. 3. (left) The model regional Arctic domain and (right) map of the Chukchi Sea. Long curving arrows show schematic flows of Pacific Water from the Chukchi Sea into the interior of the Arctic Ocean through BC, CC, and HC. Vertical black lines show gates BC and CC + HC, which will be used for flux calculations. Isobaths (m) are contoured.

Note that the sea ice on the Chukchi Shelf is seasonal with ice concentration ranging from 0% during the summer to 95%–100% during the winter. Hence, these start dates are attempts to pick out the first date of the freezing season. In our analysis, we use a start date that corresponds to a sea ice concentration of 95% and will investigate the sensitivity of ice production to this start date definition by varying sea ice concentration between 90% and 99%. We also define the end of the sea ice production season as when heat loss from the ocean to the atmosphere is less than 20 W m^{-2} . In the simulation, sea ice on the Chukchi Shelf typically reaches 95% concentration during the third week of December. During each winter, sea ice volume production V_i and salt release Salt_F are obtained from the daily heat loss H_L (Joules) as follows:

$$V_i = H_L \rho_i^{-1} L^{-1} \quad \text{and} \quad (1)$$

$$\text{Salt}_F = \rho_i V_i (S_w - S_i), \quad (2)$$

where H_L is either obtained from the net JRA25 ocean-to-atmosphere heat flux or from the model output, ρ_i is the ice density ($0.92 \times 10^3 \text{ kg m}^{-3}$), L is the latent heat of fusion ($3.34 \times 10^5 \text{ J kg}^{-1}$), S_w is the salt-water salinity, and S_i is the sea ice salinity. The two different ways of obtaining H_L offer insight into differences between model and SSM/I sea ice and open water conditions. In the model, S_i is set to ~ 10 psu (Nguyen et al. 2011). In their calculation, CM94 increased the heat loss to take into account a lower L_i due to $S_i > 0$ [see Eq. (2) in CM94]. In our model, however, we did not parameterize L_i as

a function of S_i . As a result, we did not increase the heat loss the way CM94 did; if we had done so, sea ice production would have been higher. We discuss the effect of this higher heat loss on sea ice production in section 3a(1).

Figure 4a shows the nine regions used for comparison with sea ice production estimated from CM94. These 9 regions span approximately the same area as the 23 regions used in CM94. In addition, we evaluate ice production along the Alaskan coast in the Chukchi Sea (region 1) with that from the more recent estimates, which are calculated using a more sophisticated procedure and are based on SSM/I and Advanced Microwave Scanning Radiometer (AMSR) data (Martin et al. 2004, 2005).

2) DENSE WATER AND UPPER HALOCLINE WATER CALCULATIONS

DW and UHW productions described here are based on the ice production rate above and follow the CM94 procedure. To calculate DW production, CM94 needed the surface salinity S_o and DW salinity S_d (assumptions 2 and 3). For S_o , CM94 used a compilation of in situ observations and assigned three values in each region to cover the observed variability in the data. For S_d , due to the lack of observations, CM94 assumed two different values: 1.5 and 2.0 psu higher than S_o . Values calculated from the CM94 late start date, intermediate S_o , and averaged over the two S_d are used in this study for comparison.

For the model calculations, with available outputs of T - S , the CM94 assumption for S_d is not necessary. Following CM94, the model-based calculation of DW volume V_d is

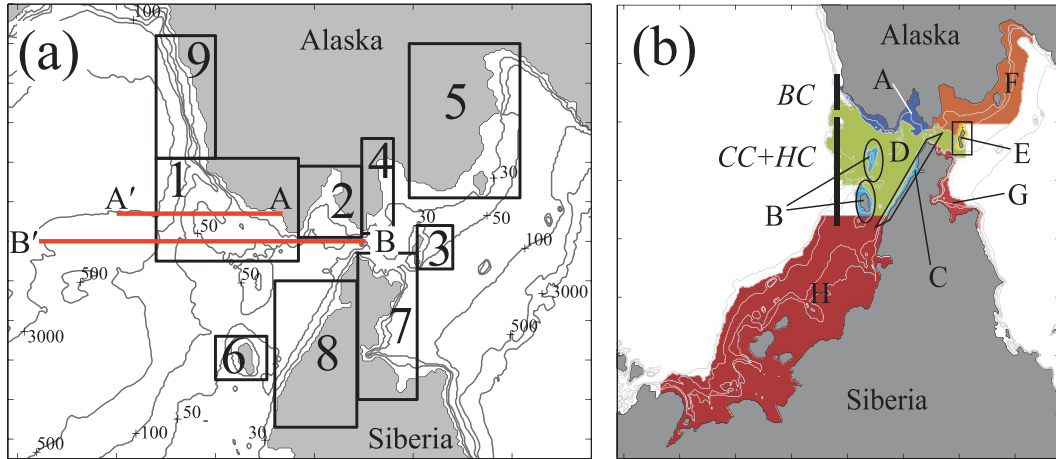


FIG. 4. Maps of the Chukchi Sea showing (a) the nine regions CM94 used to calculate DW production from polynya-related events and (b) the eight locations of passive tracers used in the 9-km simulation. Tracers A–C and E–F in (b) overlaps with the nine regions CM94 used in (a). In addition, tracers D and H are used to track winter-transformed Pacific Water. Isobaths (m) are contoured in (a). The coastline and land mask are at the model grid spacing. See Figs. 7–9 for vertical hydrographic structure of sections AA' and BB'.

$$V_d = \rho_i V_i (S_o - S_i) (\rho_d S_d - \rho_o S_o)^{-1}, \quad (3)$$

where ρ_d is the density of DW and ρ_o the density of ambient water. As defined in CM94, V_d is the DW with salinity ranging from 1.5 to 2 psu higher than the background water's salinity that is available to mix with ambient water to produce UHW (what we call dense water in Fig. 1). In the model-based calculations, S_o is estimated within each region using the mean 1993–2008 salinity in the first three layers (centered at the 5-, 15-, and 25-m depths) for the following reasons: First, we want to reproduce the CM94 method, which includes an assumption about mean background salinity within each region; CM94 used regional-mean values based on in situ observations, and we use regional-mean values based on the model output of salinity. Second, the Chukchi Shelf is ~ 50 m deep (i.e., five model vertical levels) and, as we will show later in the analysis, the bottom two layers in the model tend to contain the newly formed DW. As a result, we use the top three layers to calculate the mean regional background salinity. This salinity range will also allow us to look at the sensitivity of DW production as a function of assumed S_o in section 3a(3). To further quantify the fractional DW production, we separate V_d into five categories of potential density anomaly at increments $\Delta\sigma$ of 0.2 kg m^{-3} .

For upper halocline water (Fig. 1), we use a model's core salinity of $S_{\text{UHW}} = 32.85$ psu, which is the same as that used in CM94 (assumption 4). This value of S_{UHW} is obtained from the minimum salinity between 32 and 33.5 psu in the Canada Basin T – S diagram in Fig. 2b and follows the definition of UHW water in Fig. 1. We also

vary this basinwide-mean UHW core salinity by $\pm 1\%$ and discuss sensitivity of DW production to S_{UHW} variations in section 3a(3).

The volume of upper halocline water V_{UHW} is calculated using a mixing formulation with V_d and V_o as end members as follows (Tomczak 1981):

$$V_{\text{UHW}} S_{\text{UHW}} = V_d S_d + V_o S_o, \quad (4)$$

where V_o is the volume of the ambient water in Fig. 1 with salinity S_o and $V_{\text{UHW}} = V_d + V_o$. In the case where $S_d < S_{\text{UHW}}$, CM94 assumed that $S_d = S_{\text{UHW}}$ and calculate V_{UHW} as (assumption 5)

$$V_{\text{UHW}} = \rho_i V_i (S_o - S_i) (\rho_{\text{UHW}} S_{\text{UHW}} - \rho_o S_o)^{-1}. \quad (5)$$

It will be shown that the inclusion–exclusion of the contribution from Eq. (5) approximately corresponds to the inclusion–exclusion of the contribution from the smallest $\Delta\sigma$ of DW. Uncertainties in V_d and V_{UHW} are estimated from the range of S_o and S_{UHW} used [section 3a(3)].

3) MODEL SKILL MEASUREMENT

To quantitatively evaluate the model sea ice, DW, and UHW productions, we use the root-mean-square error (RMSE) as defined in Oke et al. (2002),

$$\begin{aligned} (\text{RMSE})^2 &= N^{-1} \sum_{i=1}^N (m_i - o_i)^2 \\ &= (\bar{m} - \bar{o})^2 + (s_m - s_o)^2 + 2s_m s_o (1 - r) \\ &= (\text{MB})^2 + (\text{SDE})^2 + 2s_m s_o (1 - r), \end{aligned} \quad (6)$$

where m_i and o_i are modeled and satellite-derived values, the overbar denotes the time mean, s_m and s_o are the model and satellite-derived sample standard deviations, r is the correlation coefficient defined as $r = s_m^{-1} s_o^{-1} N^{-1} \sum_{i=1}^N (m_i - \bar{m})(o_i - \bar{o})$, and N is the number of overlapping years of the modeled and satellite-derived ice production time series. Equation (6) shows that the mean of misfit (model minus data) squared (RMSE)² can be decomposed into three terms related to the mean model bias (MB), the error in variability SDE, and the correlation error $1 - r$ (Oke et al. 2002).

For ice production in region 1, in addition to comparing satellite derived (o_i ; Martin et al. 2004, 2005) with estimates from both the model (m_i) and JRA25–SSM/I (m_i), we also compare the model production to that computed from JRA25–SSM/I. Because JRA25 forcing is used in both the JRA25–SSM/I and the model ice production computations, we expect the two to be highly correlated except in the case when the model is adjusting during initial state or when the model ice cover is drastically different from SSM/I concentration.

c. Model numerical calculations and tracer setup

Here we described DW and UHW production calculations using the model 3-day average of T–S and passive tracers. Eight passive tracers in the 9-km configuration as shown in Fig. 4b are used to calculate DW and UHW productions. Initial locations of the passive tracers are constrained by the bathymetry as follows: tracer A covers the eastern Chukchi Shelf and is confined to depths above 30 m; tracer B covers shallow water above 30 m surrounding Herald Shoal and Wrangel Island; tracer C hugs the eastern Siberian coast just north of Bering Strait above the 30-m depth; tracer D covers the rest of the Chukchi Shelf below 30 m; tracer E covers the area shallower than 25 m surrounding the St. Lawrence Island; tracer F covers Norton Sound at depths shallower than 30 m; tracer G covers the Gulf of Anadyr in the northern Bering Sea above 40 m; and tracer H covers the Laptev and east Siberian shelves above 30-m depth. These locations are related to the nine regions covered in CM94 (Fig. 4a) as follows: Tracers A–C and E–G overlap with the nine above-mentioned regions and encompass the areas where CM94 deemed polynyas most likely to occur. In addition, tracers D and H cover locations where winter-transformed water most likely forms. These eight tracers are injected only in the model surface level at each model time step. Thus, any tracer seen at depth reflects the sinking of DW. DW within the tracers is further constrained with mean temperature $T < -1.3^\circ\text{C}$ and $S > 32.3$ psu ($\sigma \sim 26 \text{ kg m}^{-3}$). Finally, UHW flux is calculated as the volume of DW,

which flows downslope below the 50-m depth in Barrow Canyon and the combined Central and Herald Canyons (Fig. 4b).

To investigate the contribution of eddy transport to UHW ventilation, we calculate eddy and mean fluxes using 3-day average ocean T–S and velocity fields from the 4-km configuration as follows,

$$\overline{u' C'} = \overline{u C} - \bar{u} \bar{C} \quad (7)$$

where u is the total down-slope velocity, u' and \bar{u} are the eddy and mean components with $u \equiv \bar{u} + u'$, and C is the DW property (density, salinity, temperature). As is the case in the 9-km configuration, DW is constrained to $T < -1.3^\circ\text{C}$ and $S > 32.3$ psu ($\sigma > 26.0 \text{ kg m}^{-3}$). Temporal averaging periods ranging from 1 month to 1 yr are used to calculate the mean fields in order to investigate the time at which the mean and eddy transports are stable.

3. Results and discussion

In this section we first compare polynya, sea ice, DW, and UHW productions following the CM94 procedure with estimates from the satellite-derived ice productions of Martin et al. (2004, 2005) and of CM94. A discussion of DW production based on the 9- and 4-km model T–S and velocity fields follows. The seasonal cycle of DW formation in both the 9- and 4-km simulations is also compared. Finally, we show UHW mean and eddy transport from the shelf break into the Canada Basin interior from the 4-km simulation. The time scale of halocline ventilation will also be estimated.

a. Results based on CM94 calculations

1) SEA ICE PRODUCTION

A 1993–2008 time series of net sea ice production along the Alaskan coast in the Chukchi Sea (region 1), as obtained from Eq. (1) is shown in Fig. 5a. The error bars in Fig. 5a show the range when the sea ice concentration, which is used to define the start date of each winter season, is between 90% and 99%. In the same figure, we also show recent satellite-derived estimates from Martin et al. (2004, 2005). The wind condition near the coast of Alaska plays an important role in driving sea ice offshore and dictates the rate of polynya formation (Pickart et al. 2005; Martin et al. 2005). This gives rise to the large interannual variability in sea ice productions seen in Fig. 5a. Prior to 1999, the model underestimates the satellite-derived sea ice production variability (Fig. 5a).

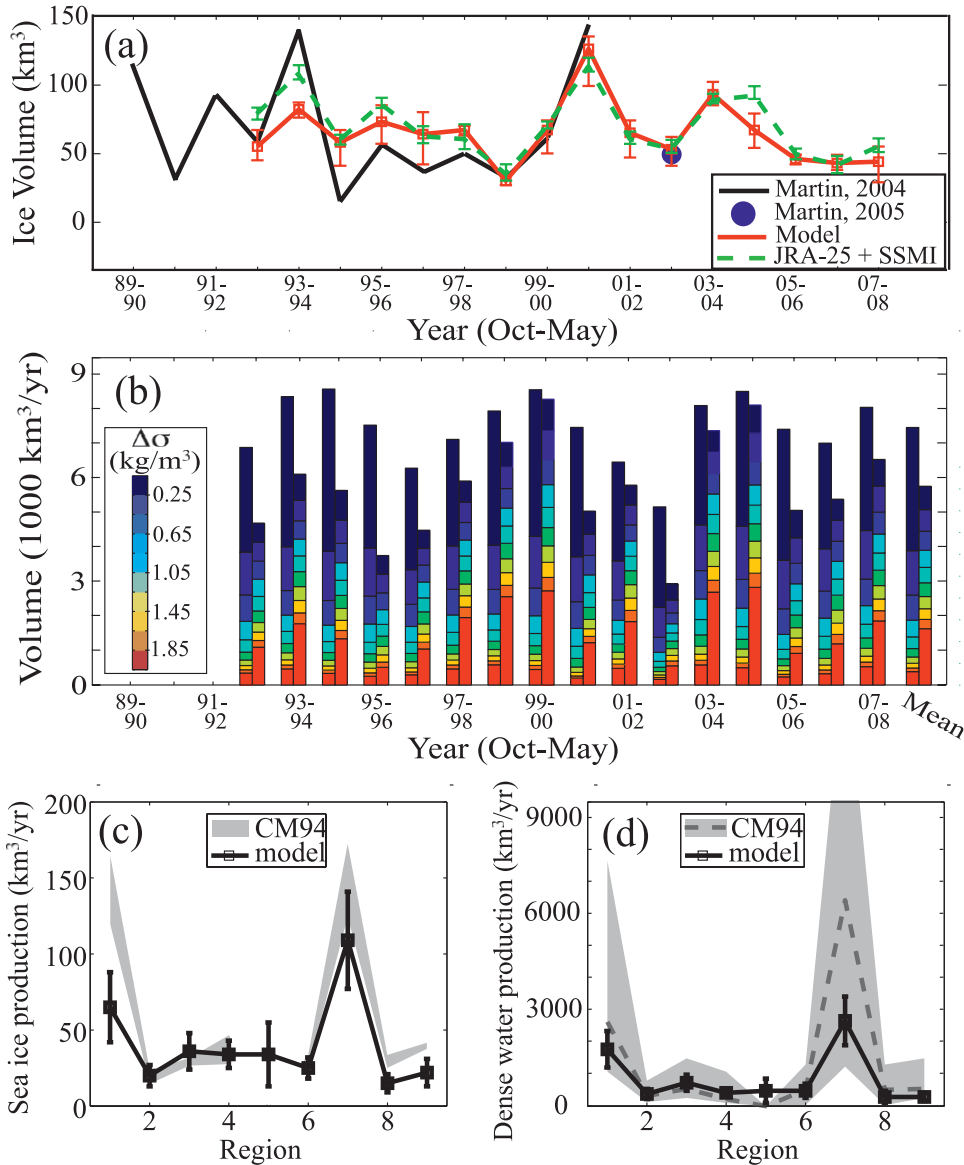


FIG. 5. (a) Net October–May sea ice production in region 1 for the period 1993–2008; (b) net DW (left) and UHW (right) production; and comparison of (c) sea ice and (d) DW productions to CM94 values for the nine regions shown in Fig. 4. See section 3a(3) for discussion of errors in the sea ice production calculations. In (b), the left and right columns are yearly DW and UHW volume production as calculated following CM94. The color scale in (b) shows contributions to the annual volumes from each density bin. Here, $\Delta\sigma$ is the increment in density compared to ambient surface density S_0 in each region. The shaded ranges in (c) and (d) are CM94 values for early and late start dates.

The first three rows of Table 1 list values for RMSE, correlation coefficient r , and the three terms in Eq. (6) for ice production in region 1 during the 1995–2003 period, which is the overlapping period between modeled and satellite-derived ice production, excluding the first 2 yr of model adjustment. All time series have high correlation coefficients with each other with $r \geq 0.85$. As anticipated, the model variability matches that of JRA25–SSM/I with the lowest SDE of 4 and highest

correlation coefficient $r = 0.97$. In addition, there is only a very small bias ($MB = 1$) between JRA25–SSM/I and the model, implying that the model sea ice coverage matches that from SSM/I very well. Compared to satellite-derived production, however, both the model and JRA25–SSM/I overestimate production by 12–13 $\text{kg}^3 \text{yr}^{-1}$. In addition, both the model and JRA25–SSM/I underestimate the variability (SDE of -11 to -14 ; see also Fig. 5a). If we increase heat loss to account

TABLE 1. Model skill measurement of sea ice and DW productions for the period 1995–2008, following Eq. (6). All terms have units of $\text{km}^3 \text{yr}^{-1}$, except for the cross correlation r , which is unitless.

Region 1 sea ice production, 1995–2003											
m	o	N	\bar{m}	\bar{o}	s_m	s_o	RMSE*	MB	SDE	r	r error
Model 9 km	M04, M05**	8	67	54	25	36	22 (27)	13	–11	0.90	14
JRA25–SSM/I	M04, M05	8	66	54	22	36	24 (25)	12	–14	0.85	15
Model 9 km	JRA25–SSM/I	8	67	66	25	22	7 (12)	1	4	0.97	6
Regions 1–4 and 6–9 sea ice production											
m_1	m_2	N	\bar{m}_1	\bar{m}_2	s_{m1}	s_{m2}	RMSE	MB	SDE	r	r error
Model 9 km	CM94	8	41	69	30	58	44	–28	–29	0.92	17
Regions 1–4 and 6–9 DW production											
Model 9 km	CM94	8	28	46	26	64	43	–19	–38	0.96	11

* Values in parenthesis are for period 1993–2003.

** Martin et al. (2004, 2005).

for the dependence of L_i on S_i in Eq. (1), MB would increase to ~ 28 , but SDE would remain approximately the same at -9 . The consistent overestimation of the mean and underestimation of variability in the model and JRA25–SSM/I compared to satellite-derived values suggests a common issue related to the JRA25 forcing. However, the overall high correlation in sea ice production between this study and Martin et al. (2004, 2005), which is based on calculations of heat loss in polynyas, suggests that sea ice between Cape Lisburne and Point Barrow in the Chukchi Sea is produced primarily during polynya events.

Table 1 (last two rows), Table 2, and Fig. 5c summarize the statistics and annual sea ice production in all nine regions shown in Fig. 4a. Error bars in Fig. 5c show the interannual variability around the 1993–2008 mean. Note that, because CM94 is an alternate method for estimating sea ice, we relabel the model and CM94 as m_1 and m_2 , respectively, in place of m and o in Eq. (6). The correlation in ice production between the model and the CM94 estimates is 0.92. In both model and CM94, ice production is largest in the Gulf of Anadyr (region 7), a result of prevailing northeasterly wind that pushes sea

TABLE 2. Annual-mean 1993–2008 sea ice, DW, and UHW production. Estimates are based on the CM94 procedure. SUM₁ reflects total production where contribution from the first $\Delta\sigma$ bin is excluded.

Region	Model (1993–2008)				CM94 (1978–86)			
	S^a	Sea ice (km ³)	DW (km ³ yr ⁻¹)	UHW (km ³ yr ⁻¹)	Box	S^b	Sea ice ^c (km ³)	DW ^d (km ³ yr ⁻¹)
1	31.4	65 ± 23 ^e	1770 ± 570	540 ± 250	3–6	31.5	120–165	1860–2620
2	30.7	20 ± 7	380 ± 160	130 ± 60	1–2	31.1	15–24	190–320
3	31.3	36 ± 12	730 ± 250	380 ± 160	19–20	31.9	27–32	440–540
4	29.3	34 ± 9	410 ± 95	130 ± 60	24–26	29.2	28–47	130–220
5	30.1	34 ± 21	470 ± 380	130 ± 130	—	—	—	—
6	31.3	25 ± 7	470 ± 220	190 ± 95	10–11	30.5	25–34 ^f	360–510
7	32.3	109 ± 32	2650 ± 760	4070 ± 1420	21–23	32.8	125–173	4620–6410
8	31.4	15 ± 6	280 ± 190	130 ± 130	7–9	30.8	26–34	360–510
9	29.9	22 ± 9	280 ± 130	60 ± 30	12–16	31.2	38–42	470–540
SUM		359 ± 49	7450 ± 1100	5740 ± 1420			404–551	8430–11650
SUM ₁			3880 ± 630	5050 ± 1360				
Uncertainty ^g		14%	20%	55%				33%

^a Mean 1993–2008 salinity in the upper 30 m.

^b Intermediate surface salinity.

^c Ranges are based on early and late winter starting dates.

^d Based on sea ice and averaged over the two CM94 values for S_d . See section 3a(2) for discussion.

^e ± values reflect the interannual variability around the 1993–2008 mean.

^f CM94 provided combined estimates for boxes 7–11 and 30. Here we split the estimates from boxes 7–11 into our regions 6 and 8.

^g Values reported here are cumulative uncertainties when additional factors are taken into consideration. See section 3a(3) for further discussion.

ice away from the coast in this area (CM94). Overall, the net ice production from the model ($359 \pm 49 \text{ km}^3 \text{ yr}^{-1}$) is lower than the CM94 estimate ($404 \text{ km}^3 \text{ yr}^{-1}$; Table 2), which resulted in negative MB and SDE (fourth row in Table 1). Along the Alaskan coast (region 1), our estimate of $65 \pm 23 \text{ km}^3 \text{ yr}^{-1}$ agrees with that from Martin et al. (2004, 2005) of $67 \pm 42 \text{ km}^3 \text{ yr}^{-1}$ but is significantly less than the CM94 values ($120\text{--}165 \text{ km}^3 \text{ yr}^{-1}$; Table 2). If we take into account the dependence of L_i on S_i in Eq. (1), the model ice production for this region would increase to $\sim 85 \text{ km}^3 \text{ yr}^{-1}$, which is still significantly lower than CM94 values. CM94 estimated errors in ice production in this area of $30\text{--}40 \text{ km}^3 \text{ yr}^{-1}$, which potentially bring their lower estimate for the region to $\sim 80 \text{ km}^3 \text{ yr}^{-1}$. For comparison, Winsor and Björk (2000) calculated a significantly lower rate of $12.1 \text{ km}^3 \text{ yr}^{-1}$ for this same region over 39 winter seasons from 1958 to 1997 using a polynya model forced by NCEP. It is unclear why their values are significantly lower than Martin et al. (2004); they speculated that it may be due to errors in open water identification in SSM/I concentration.

2) DW AND UHW PRODUCTION

Net DW production in all nine regions, as calculated using sea ice production described above and following Eq. (3), is summarized in Tables 1 and 2 and shown in Fig. 5b. Nearly half of the DW produced during each winter is within the range $0.05\text{--}0.25 \text{ kg m}^{-3}$ (i.e., the first density bin $\Delta\sigma_1$). Note that these $\Delta\sigma$ ranges are defined in reference to the ambient water with average salinity shown in Table 2 (second column). This means that, in all nine regions, water within $\Delta\sigma_1$ corresponds to that with $S < S_{\text{UHW}}$. If we exclude CM94's assumption in Eq. (5) (i.e., consider that DW within $\Delta\sigma_1$ is not dense enough to contribute to the total halocline water production and exclude it), the annual-mean DW production over the 1993–2008 period is $3880 \pm 630 \text{ km}^3 \text{ yr}^{-1}$ (SUM₁ in Table 2). Following Eqs. (4) and (5), over the same period, local mixing yields UHW production of $5740 \pm 1420 \text{ km}^3 \text{ yr}^{-1}$ with $\Delta\sigma_1$ included and $5050 \pm 1360 \text{ km}^3 \text{ yr}^{-1}$ with $\Delta\sigma_1$ excluded.

A region-by-region comparison with CM94 is shown in Fig. 5d. Shaded area in Fig. 5d covers the upper and lower limits of the assumed surface salinities in CM94. Error bars in both Table 2 and Fig. 5d are the interannual variability around the 1993–2008 mean values. Similar to the sea ice production, the model mean and variability of DW across all regions are lower than those from CM94 (MB = -19 and SDE = -38) primarily due to lower values in regions 1 and 7 (Fig. 5d). The high correlation of 0.96 between the model and CM94 is not unexpected because of the high correlation in ice productions and because we followed the CM94 procedure

to calculate DW. It remains to be seen if these DW production rates are consistent with estimates from model numerical calculations using the model output of water properties in the next subsection.

3) UNCERTAINTY ESTIMATES

Here we discuss (i) the sensitivity of sea ice production to winter starting date and (ii) the sensitivity of DW and UHW production to surface water salinity S_o , surface temperature, and UHW core salinity S_{UHW} . CM94 selected an early and a late winter start date to assess the variability in sea ice production. In this study, we define the start of winter as when sea ice concentration reaches 95%. A lower or higher concentration directly corresponds to redefining the start of the winter season at an earlier or later date and yields a higher or lower sea ice production, respectively. To examine the sensitivity of production based on this assumption, we calculate the upper and lower bounds in production using 90% and 99% sea ice concentration. Sensitivity of sea ice production to end date definition is lower than sensitivity to start date definition. The end date is chosen when net heat loss from ocean to the atmosphere is -20 W m^{-2} . This relatively small heat loss, combined with reduced sea ice concentration and thickness in the seasonal ice zone at this time of year, means that ice growth and brine rejection are relatively small near the end date compared to starting date. The error bars in Fig. 5a (red curve) and in Table 2 (third column) reflect the sensitivity of sea ice production to the 90%–99% sea ice concentration range. For the entire western Arctic (i.e., the combined nine regions in Fig. 4), the uncertainty is approximately 14% of the net sea ice production (error bars in Fig. 5c).

For DW calculation, CM94 estimated that a 1% change in S_o and a 5% change in sea ice concentration correspond to 23% and 7% changes in the DW production, respectively. In the simulation, net DW production varies within 15% of the mean because of variations in S_o in the top three layers ($\pm 1100 \text{ km}^3 \text{ yr}^{-1}$; Table 2, fourth column). If we include the 14% sea ice production uncertainty from above, the net uncertainty in DW production is $\sim 20\%$ (Table 2, fourth column).

For UHW production rate, the sensitivity of UHW is $\sim 50\%$ for a 1% (0.3 psu) change in S_{UHW} . If we allow for this 1% of S_{UHW} uncertainty, the combined uncertainty is 54% (50% from S_{UHW} and 20% from DW as discussed above assuming uncorrelated errors; bottom row in Table 2). Therefore, the UHW production rate uncertainty in the CM94 procedure is dominated by the S_{UHW} uncertainty.

b. Model results

We first show the seasonal cycle of DW formation and UHW ventilation. Production rates of DW and UHW

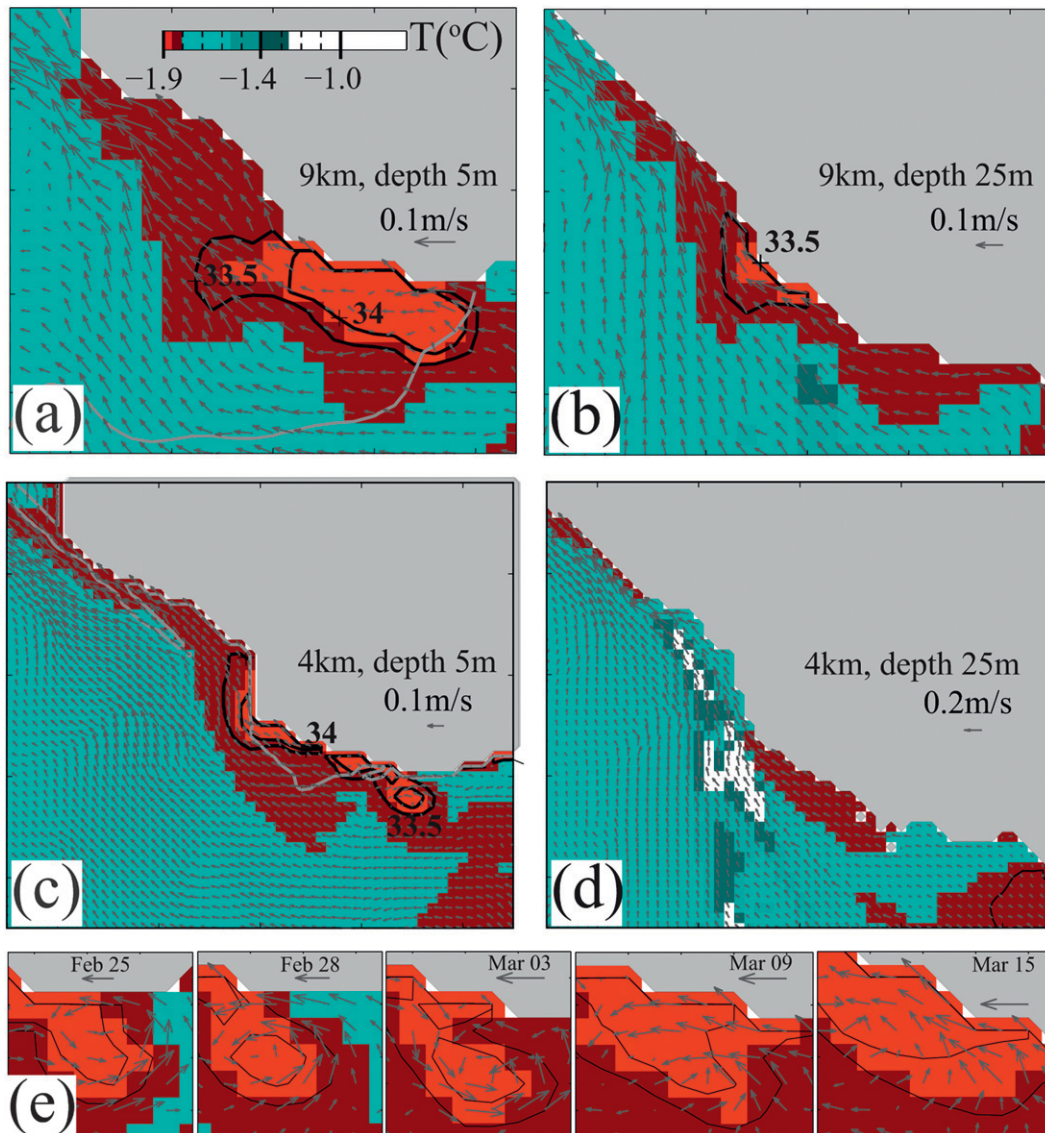


FIG. 6. Map view of polynya-related DW forming between Cape Lisburne and Point Barrow on 28 Feb 1998 in (a),(b) the 9-km simulation and (c),(d) the 4-km simulation and (e) the evolution of an eddy, which is seen next to the surface-level 33.5-psu contour label in (c). The color scale shows potential temperature. Thick gray contours in (a),(c) show the 95% sea ice concentration and black contours in all panels show sea salinity $S > 33.5$ psu. Velocity vectors shown are 3-day averages in (a)–(d) and anomalies with the monthly-mean removed in (e). The length of each velocity vector underneath the date labels in (e) corresponds to 0.05 m s^{-1} . The surface-level eddy in (e) travels ~ 48 km from 25 Feb to 15 Mar as it loses its coherent structure and merges with the larger salinity anomaly.

from both the 9- and 4-km simulations follow. Finally, we discuss the contribution of eddy transport to the net DW flow on the shelf and in the Canada Basin interior.

1) SEASONAL CYCLE OF DW FORMATION AND UHW VENTILATION

During the winter months, in addition to winter-transformed water on the Chukchi Shelf, polynya events such as the one shown in Figs. 6a–c often develop along the coast. These events can produce highly salty and DW

($T < -1.8^\circ\text{C}$, $S > 34$ psu, and $\sigma > 27.25 \text{ kg m}^{-3}$) in the upper 30 m in the model. Below 30 m, maximum salinity is typically 1 psu lower. At 4-km resolution, the model just begins to resolve the shelf eddies predicted by GC95 and CG95. A closer look at the feature with concentric salinity contours in Fig. 6c shows a surface-level cyclonic eddy that formed on 22 February 1998. Between 28 February and 3 March 1998, the eddy is first seen detaching from the main source before merging with an existing salinity anomaly and getting advected

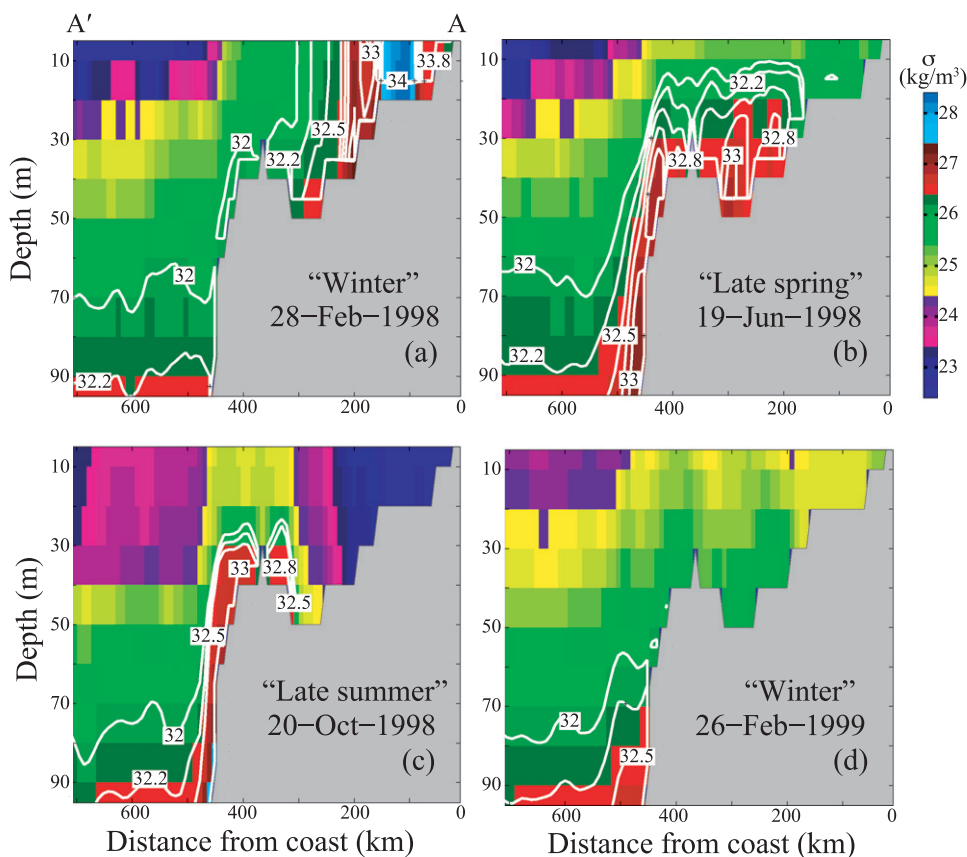


FIG. 7. Vertical section along line AA' in the 9-km simulation showing typical seasonal distributions of DW with depth (see Fig. 4 for location of line AA'). Hypersaline water, which forms during polynya events, has salinity ~ 34 psu and potential density $\sigma > 27.4$ kg m^{-3} . The color scale chosen here is meant to highlight the hypersaline water (shades of cyan), DW and its path (dark green and shades of red), and ambient water (shades of blue and magenta). Salinity (psu) are contoured.

downstream. The total distance the eddy traveled along the coast before losing its characteristics is ~ 48 km (12 grid points). Both the eddy's growth rate of ~ 6 days and length scale of 30 km (in diameter) are consistent with those predicted in theoretical calculations. GC95 estimated eddies transporting DW to the shelf slope at a mean speed of ~ 0.02 m s^{-1} . We note, however, that GC95 and CG95 did not consider DW formation within a strong spatially varying flow or with realistic, spatially varying bathymetry. When there is a strong alongshore current and a submarine parallel to the main flow direction, Chapman (2000) showed that a substantial amount of DW can get advected into the canyon. In the 4-km simulation, the along-shelf mean flow, on the order of 0.05 – 0.1 m s^{-1} , is the primary mechanism of DW advection to the canyons.

Figures 7 and 8 show the T – S – σ vertical structure of section AA', which runs through the center of the polynya shown in Fig. 6a. On 28 February 1998, the vertical extent of hypersaline water is seen down to the bottom

of the 20-m shallow shelf. The main qualitative difference between the 9- and 4-km solutions is in the horizontal extent of the densest water (e.g., $\sigma > 27.4$ kg m^{-3} in Figs. 7a, 8a). Because of local mixing and advection, areas surrounding and downstream of the polynya also have relatively high salinity–density. By 19 June 1998, bottom-trapped dense shelf water is seen flowing down the slope in both 9- and 4-km vertical sections, and middepth (70–120 m) salinity contours of 32–33 psu are seen extending onto the shelf (Figs. 7b, 8b). This result is consistent those of Gawarkiewicz (2000) for the case of high salinity gradient offshore (e.g., his Fig. 11a for day 70). By 20 October 1998, small remnant of DW, which is transported northward from the Bering Sea throughout the summer months, is seen flowing down the shelf slope. The large contrast in the T – S –density vertical structures between 28 February 1998 and 26 February 1999 in Figs. 7 and 8 is a manifestation of interannual variability, which we will discuss further in section 3b(2). Specifically, we will show that during the years 1999 and

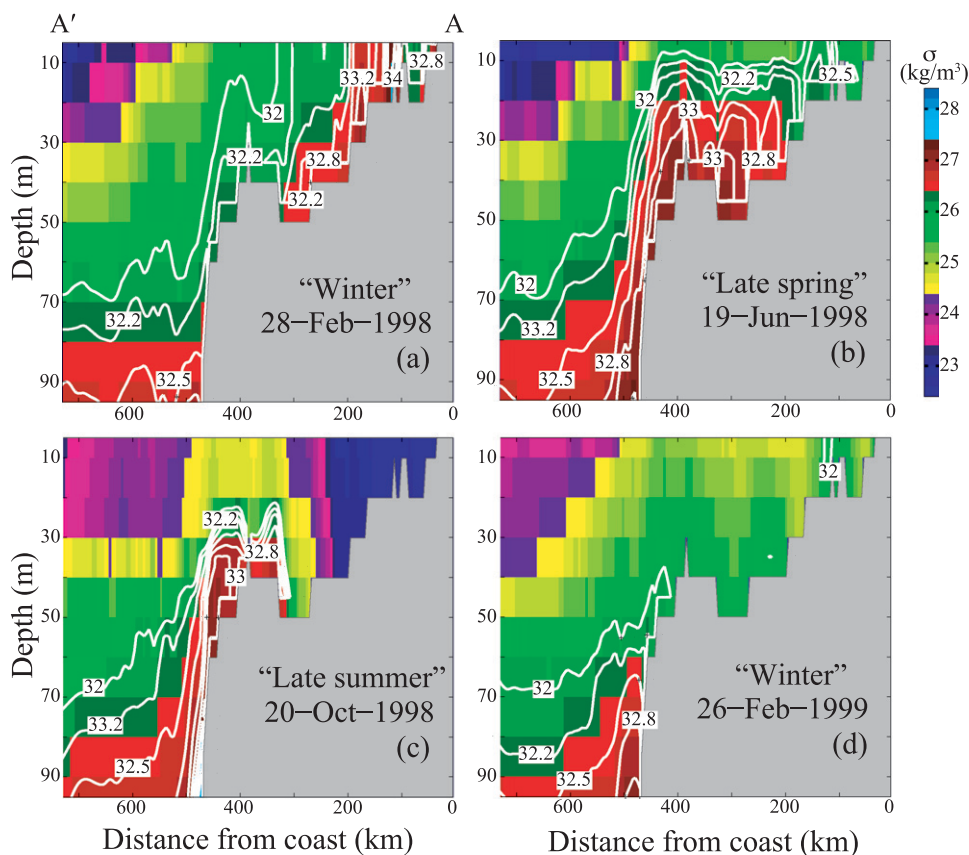


FIG. 8. Vertical section along AA' in the 4-km simulation showing typical seasonal distributions of DW with depth (see Fig. 4 for location of line AA'). Hypersaline water, which forms during polynya events, has salinity ~ 34 psu and potential density $\sigma > 27.4 \text{ kg m}^{-3}$. The color scale is as in Fig. 7.

2003 there are no significant DW transports down Barrow Canyon.

The seasonal cycle of DW formation and UHW ventilation is shown in Fig. 9 for the 9-km simulation and is based on the 1995–2008 mean vertical T–S– σ structures along profile BB'. The cycle for 4-km is similar and is not shown here. Throughout the winter, in addition to hypersaline water that forms during polynya events, winter-transformed water is also found on the Chukchi Shelf as a result of cooling and northward advection from the Bering Sea ($T < -1.6^\circ\text{C}$ in Figs. 9a,b; Pickart 2004). This cold and dense water flows down either the canyons or shelf slope to depths of 50–100 m and warms up to approximately -1.4°C as it mixes with the warmer ambient water (Fig. 9c). Seaward of the shelf break, the core UHW can be seen with temperature $T \sim -1.3^\circ\text{C}$ and $26.4 \text{ kg m}^{-3} \leq \sigma \leq 27 \text{ kg m}^{-3}$ at a depth centered at ~ 100 m (Fig. 9). The halocline depth in the model varies between 100 m near the Chukchi Cap area to 150 m in the Beaufort Sea. During the summer and fall months (July–November), water with $S < 31.5$ psu and $T > 0^\circ\text{C}$, also known as Pacific Summer Water (PSW; Woodgate

and Aagaard 2005), flows northward through Bering Strait (kilometer 0 in Fig. 9c) and slides above the bottom-trapped DW to reach the Chukchi Shelf. Throughout this time, DW continues to flow downslope while some of it mixes with the warm and fresh PSW on the shelf (Fig. 9c). In the following winter, PSW settles at a depth of ~ 40 m as surface water cools (water with $T \sim -0.8^\circ\text{C}$ in November in Fig. 9d) and the seasonal cycle restarts.

2) DW AND UHW PRODUCTIONS IN THE MODEL

To quantify off-shelf flux, we track DW using the criteria $T < -1.3^\circ\text{C}$ and $S \geq 32.3$ ($\sigma > 26.0$) in both the 9- and 4-km simulations. Figure 10 shows the 3-day average and annual flux of DW below 50 m across gates CC + HC and BC for the period 1995–2008 (see Fig. 3b for location of the gates). Three-day average velocity shows the intermittent nature of the flow down all canyons, with more bursts seen in BC for the 4-km simulation (Fig. 10b). Annual transports down CC + HC are independent of model resolution with remarkable agreements across all potential density anomaly ranges

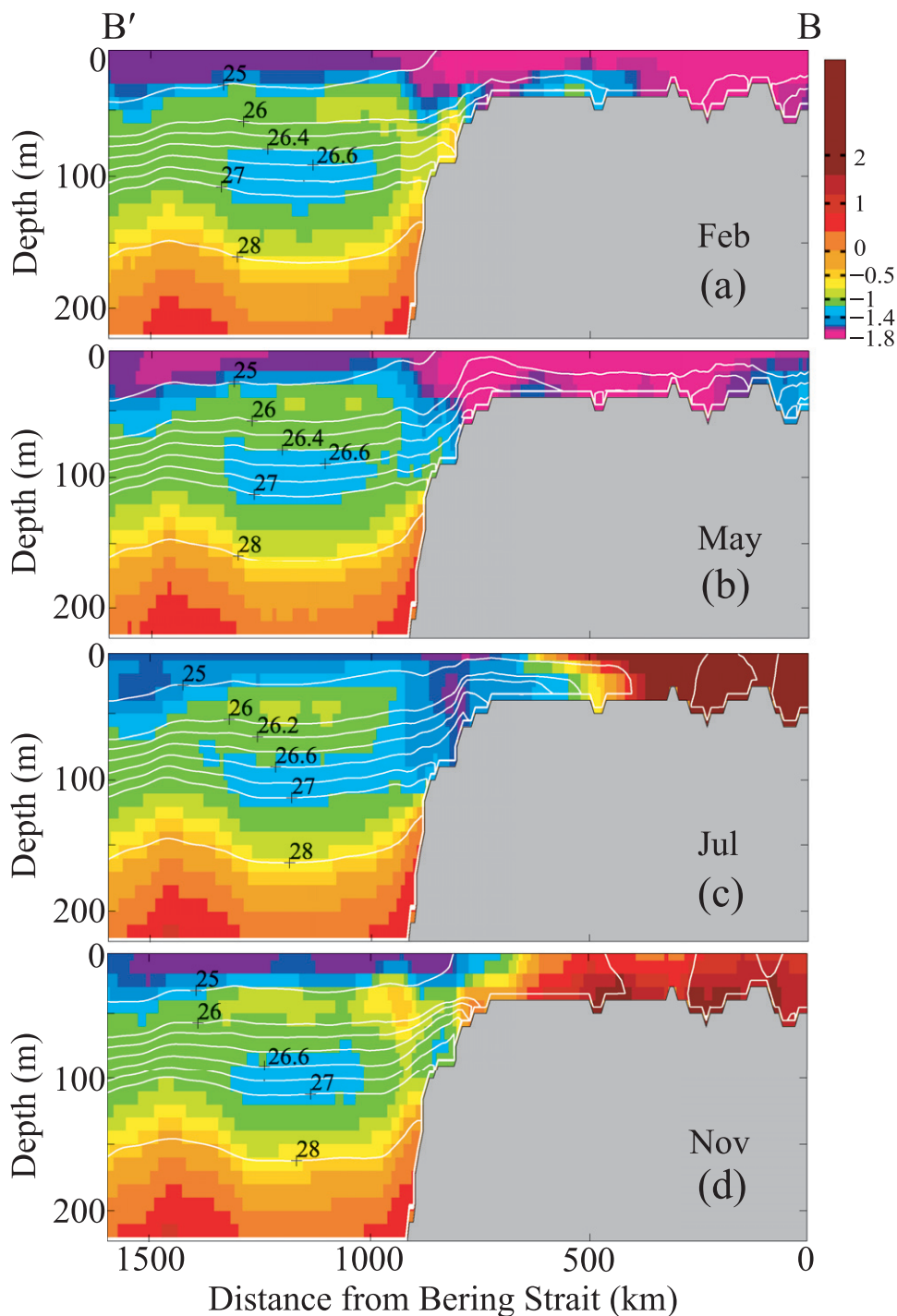


FIG. 9. The 1995–2008 mean seasonal cycle of DW along line BB' (see Fig. 4 for location of line BB'). The temperature color scale in degrees Celsius is similar to that of Pickart (2004) and shows the core temperature of the UHW in light blue at a depth of ~100 m. White contours are potential density anomaly σ in kg m^{-3} . See section 3b(1) for discussion on the seasonal cycle of DW.

$\Delta\sigma$, both in annual time series and annual-mean rates (Figs. 10a,c,d). The fractions of DW as a function of $\Delta\sigma$ are 20%, 51%–54%, 24%–27%, and 2%–3% for the four $\Delta\sigma$ shown in Fig. 10d.

For Barrow Canyon, there is a systematic difference with ~25% higher flux across all $\Delta\sigma$ in the 4-km simulation compared to the 9-km simulation (Figs. 10b,e). One possible explanation is that, at higher resolution,

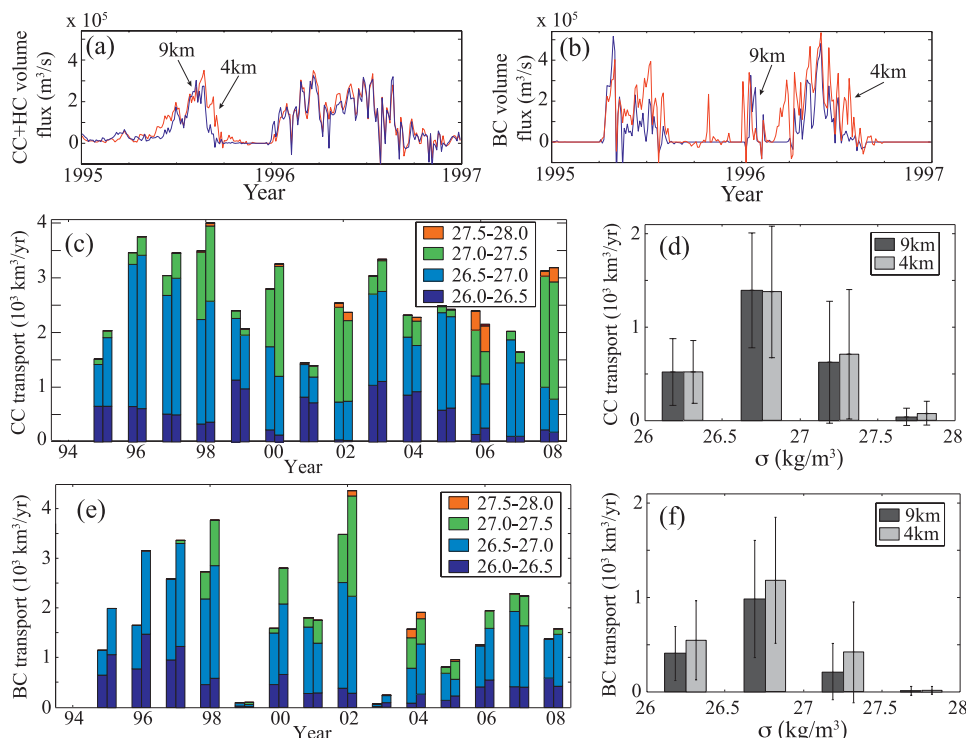


FIG. 10. Time series of 3-day average volume flux across gates (a) CC + HC and (b) BC from the 9-km (blue) and 4-km (red) simulations. Annual DW transport as a function of density for (c),(d) CC + HC and (e),(f) BC. Here, (c) and (e) show the 1995–2008 annual transport time series and (d) and (f) show the 14-yr-mean transport. In (c)–(f), transports from the 9-km simulation are shown on the left and from the 4-km simulation are shown on the right. Error bars in (d) and (f) show variability from the 14-yr mean at each σ class.

Barrow Canyon is better resolved and this allows the DW jet, which is observed by Pickart et al. (2005), to flow at a faster rate down the more confined, steeper, and narrower canyon (Wang et al. 2011) instead of being mixed horizontally. The fractional contributions are 25%, 54%–61%, 13%–20%, and <1% for the four $\Delta\sigma$ shown in Fig. 10f.

Averaged over the 1995–2008 period, DW transports across the gate BC are 1612 ± 961 and 2181 ± 1207 $\text{km}^3 \text{yr}^{-1}$ in the 9- and 4-km simulations, respectively. Transports across gate CC + HC are 2579 ± 636 $\text{km}^3 \text{yr}^{-1}$ and 2682 ± 786 $\text{km}^3 \text{yr}^{-1}$ in the 9- and 4-km simulations, respectively (Fig. 11a). These rates yield total transports of 4191 ± 1152 $\text{km}^3 \text{yr}^{-1}$ and 4863 ± 1440 $\text{km}^3 \text{yr}^{-1}$ for the two simulations, respectively. The error bars reported here represent interannual variability.

The geographic dependency of DW source and pathways is investigated with the use of eight passive tracers in the 9-km simulation, as described in section 2c. DW forms on the Chukchi Shelf throughout the winter months and begins flowing down BC typically between February and April and continues until July–August. This start date for off-shelf flows down BC is consistent

with mooring observations in Weingartner et al. (1998). Flows down CC + HC begin later, approximately in April, and end in July or August. Figure 11b shows the 1995–2008 annual-mean flux down the BC and CC + HC gates as a function of geographic source and $\Delta\sigma$. The Gulf of Anadyr in the northern Bering Sea (tracer G) contributes the largest volume of DW per unit area. This result is consistent with CM94. Overall, the Chukchi Sea (tracers A and D) contributes 56% to the total off-shelf flux across both BC and CC + HC, followed by the Gulf of Anadyr and Norton Sound (tracers G and F) at 18% and 10%, respectively (Table 3). Error bars reported in Table 3 and Fig. 11 are standard deviations of UHW production rates around its 1995–2008 mean.

A very small amount of DW (24 ± 14 ; <1%) from the Laptev Sea and east Siberian coast (region H) is seen flowing down CC + HC or BC. A closer look shows that the water in this region is too light and stays almost entirely in the upper 50 m. We note that this result is sensitive to the freshwater input. In both the 9- and 4-km simulations, the eastern Siberian Sea and Norton Sound receive 814 and 242 $\text{km}^3 \text{yr}^{-1}$ of freshwater, respectively. As a result, the ambient water in these two regions (tracers

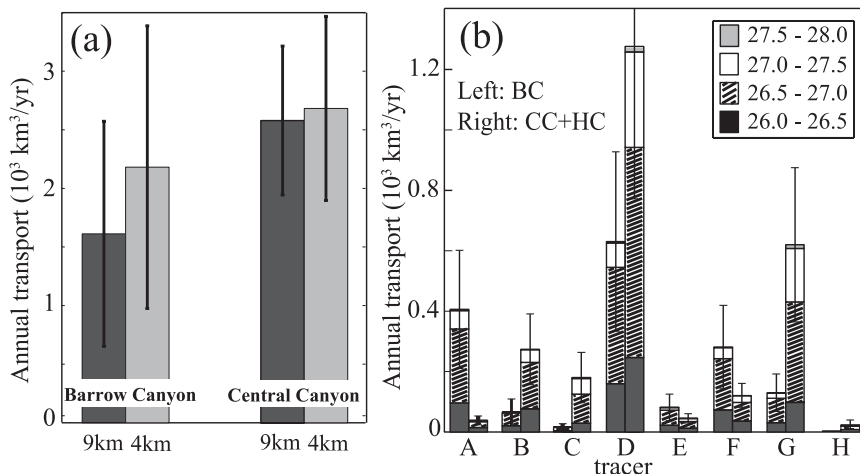


FIG. 11. (a) The 1995–2008 mean annual DW transport down BC and CC + HC as obtained from the 9- and 4-km simulations. (b) Transports down BC (left) and CC + HC (right) as a function of geographic locations. See section 3b(2) for discussion.

F and H) can be significantly fresher than the surroundings and potentially yield less brine-enriched DW.

3) MEAN AND EDDY TRANSPORTS

GC95, CG95, and Winsor and Chapman (2002) simulated eddies that (i) form on the Chukchi Shelf, (ii) peel off lenses of brine-enriched DW from the source, (iii) transport these lenses downslope, and (iv) prevent water of excessive salinity from forming on the shelf during the winter. As discussed in section 3b(1), a few (one or two per month) of the eddies mentioned in (i) and (ii) above are reproduced in the 4-km simulation to a certain extent. Based on the analysis of the 3-day average shelf velocity field (Fig. 6), however, these few surface cyclonic eddies lose their coherence a short distance downstream from the source.

Our results here are supported by some observations. For example, Danielson et al. (2006) also found

insignificant eddy activity on the shelf in the vicinity of brine-rich water in polynyas along St. Lawrence Island (see Fig. 3 for location). Their result was based on densely spaced (~10 km) mooring measurements in a field campaign, which was designed specifically to study the shelf eddy activity predicted by CG95. They suggested that the alongshore advection of DW by strong seasonal flow is the likely reason for lack of eddy activity. In addition, shears from spatially varying mean flow can potentially export DW away from the source and delay, distort, or inhibit the frontal instability growth and consequently impede the development of eddies (Danielson et al. 2006).

Farther downstream of the DW source, Chapman (2000) had shown that a combination of relatively strong mean flow and submarine canyons oriented along that mean flow direction can lead to delayed eddy development and to eddy-associated intermittent bursts of

TABLE 3. DW flux across BC and across CC + HC. Flux is in km³ yr⁻¹ and is based on 1995–2008 mean passive tracers.

Tracers	$\Delta\sigma$						Net	
	26–26.5		26.5–27.0		27.0–27.5		BC	CC + HC
	BC	CC + HC	BC	CC + HC	BC	CC + HC		
A	96 ± 62	14 ± 11	245 ± 162	20 ± 8	61 ± 90	4 ± 4	406 ± 254	38 ± 15
B	21 ± 25	77 ± 56	41 ± 36	154 ± 81	3 ± 5	42 ± 64	66 ± 56	274 ± 115
C	4 ± 5	29 ± 30	11 ± 9	97 ± 56	2 ± 3	51 ± 53	17 ± 14	180 ± 54
D	160 ± 114	247 ± 167	385 ± 247	696 ± 330	80 ± 117	315 ± 341	631 ± 383	1277 ± 349
E	22 ± 17	12 ± 8	50 ± 38	22 ± 6	9 ± 13	10 ± 11	81 ± 59	45 ± 11
F	73 ± 51	36 ± 27	170 ± 115	62 ± 14	37 ± 57	22 ± 24	281 ± 182	121 ± 26
G	31 ± 21	98 ± 73	81 ± 53	332 ± 169	17 ± 24	177 ± 174	130 ± 79	620 ± 178
H	0 ± 0	7 ± 8	0 ± 1	12 ± 10	0 ± 0	4 ± 7	1 ± 1	24 ± 15
Net	407 ± 144	520 ± 196	983 ± 326	1395 ± 384	209 ± 161	625 ± 393	1612 ± 507	2579 ± 413
Net	927 ± 243		2378 ± 504		834 ± 425			
Net	4191 ± 650							

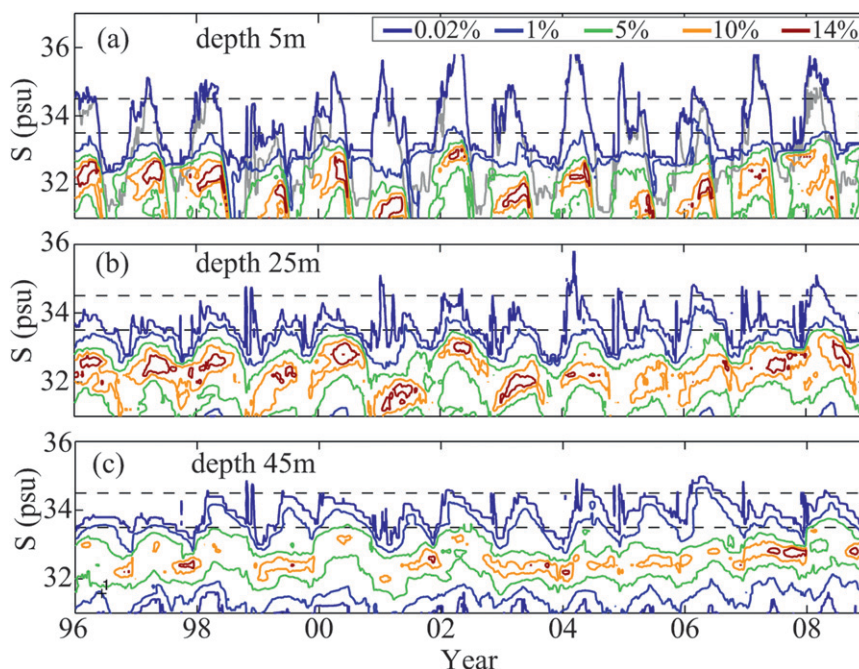


FIG. 12. Salinity frequency distribution in the Chukchi Sea in the 4-km simulation at depths of (a) 5, (b) 25, and (c) 45 m for the period 1996–2008. Dashed horizontal lines bound the salinity range 33.5–34.5 psu, which Winsor and Chapman (2002) considered for maximum shelf salinity analysis. Colored contours show the percentage of area on the Chukchi Shelf: that is, 0.02% corresponds to 0.02% of the total $\sim 445\,000\text{-km}^2$ Chukchi Sea area. The dark gray contour in (a) shows the 0.02% fractional area within region 1 (Fig. 4a) relative to the total Chukchi Sea area; it indicates that the majority of densest water formed in the Chukchi Sea came from region 1.

DW down the canyons. Thus, the intermittent flux down both CC + HC and BC in the model simulations suggests the presence of eddy activity inside these canyon (cf., e.g., Figs. 10a,b to Fig. 14b in Chapman 2000).

In addition to looking at velocity on the shelf, we examine the maximum shelf salinity as well as velocity seaward of the shelf break. Figure 12 shows salinity frequency distribution on the Chukchi Shelf. At the surface level of the model, maximum salinity in small pockets ($<0.02\%$ of the total Chukchi Sea surface area) can reach above 37 psu. Each winter, between 0% and 6% of the Chukchi Shelf surface area can have $S > 33.5$ psu and about 1% of the shelf area has $S > 34.5$ psu. These high surface salinity areas can be seen mixing down to a depth of 45 m where salinity decreases to ~ 34.5 psu (Fig. 12c). The seasonal cycle of shelf surface salinity can also be seen clearly with elevated S from the late winter to summer and reduced S close to ambient values (<31 psu) from late summer to early winter (Fig. 12a). A similar seasonal cycle is seen at depths of 25 and 45 m. At the bottom of the shelf, at depths of 45–55 m, the mean salinity is ~ 33.2 psu during the late winter to summer and 32.2 psu from fall to early winter (Fig. 12c).

The mean S of ~ 32.2 psu comes from the mixing of Pacific Summer Water and Bering Sea DW that is transported into the Chukchi Sea throughout the summer months. The maximum shelf salinity shown here is closer to values that Winsor and Chapman (2002) obtained using high-resolution meteorological forcing than to values obtained using NCEP forcing. It remains to be seen if these high salinity values are still present in coupled ocean–ice models at higher horizontal resolution than what was used here.

Seaward of the shelf break, Fig. 13 shows typical T – S and velocity fields at the mouth of Barrow Canyon at depths of 55 and 85 m in the 4-km simulation. The flow down BC has typical velocity of $0.1\text{--}0.2\text{ m s}^{-1}$ and hugs the eastern side of the canyon, consistent with the observations by Pickart et al. (2005) and with simulations by CG95. Once at the canyon mouth, at depths of 50–150 m, predominantly anticyclonic cold-core eddies with $\sim 30\text{-km}$ diameter can be seen moving lenses of cold dense water away from the shelf break into the Canada Basin (Figs. 13b,c). Eddy transports of mass, salt, and heat, as obtained from Eq. (7), are $\sim 75\%$ of the net transports into the Arctic interior. This fractional contribution is

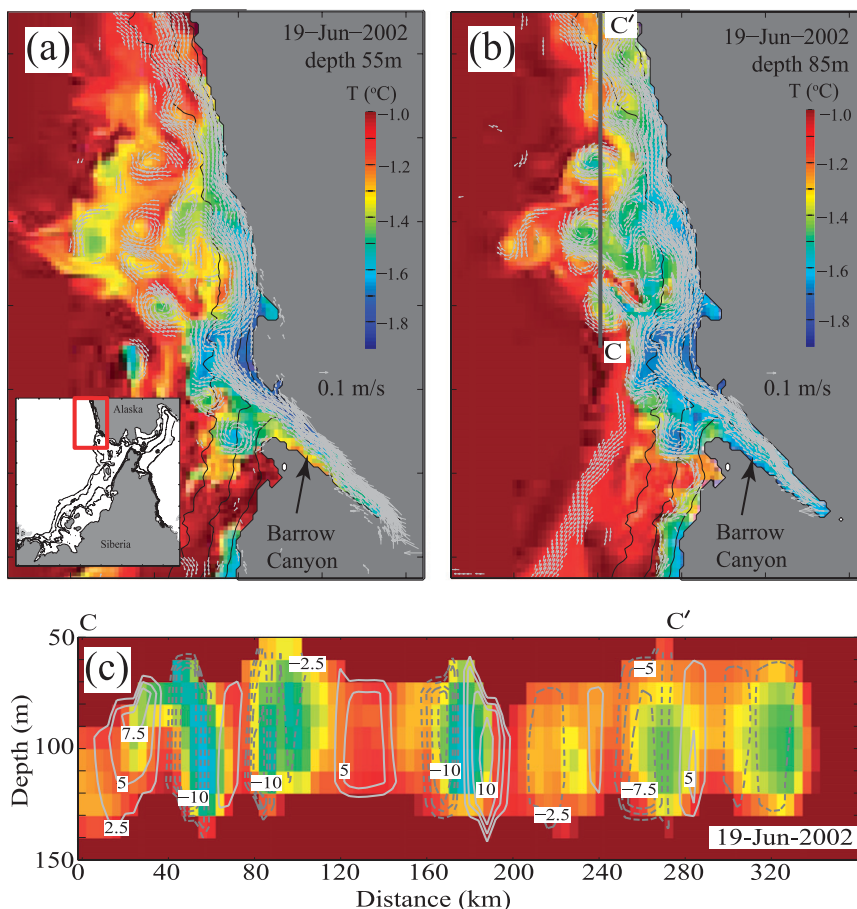


FIG. 13. The 19 Jun 2002 temperature fields inside and at the mouth of BC at depths of (a) 55 and (b) 85 m with overlaid velocity vectors. Only velocity with magnitude $\geq 0.05 \text{ m s}^{-1}$ is shown. Color scale shows temperature in degrees Celsius. (c) Vertical temperature section along profile CC' [shown in (b)] with overlaid velocity anomaly contours in cm s^{-1} . A seasonal-mean velocity of -0.45 cm s^{-1} (June–August 2002) was removed. Negative velocity (dashed contour) is northward. The color scale is the same as that in (b). Inset in (a) is a map of the western Arctic Ocean with the red box showing locations of maps in both (a) and (b).

consistent across several averaging periods ranging from 1 month to 1 yr. A drift in eddy transport exists with 60%–70% contribution between 1995 and 2002 and 80%–90% between 2003 and 2008. For comparison, Spall et al. (2008), who advected DW down Barrow Canyon to achieve the observed flow rate from Pickart et al. (2005), showed in their 1-km idealized simulation that 100–200 predominantly anticyclonic cold-core eddies form each year seaward of the shelf break, at depths of 50–150 m, and transport nearly half of the shelf water into the basin interior.

In summary, the 4-km simulation produces a small number of localized eddies on the shelf with growth rate and length scale consistent with those predicted in GC95 and CG95. These eddies, however, lose their coherent structures a short distance downstream from the source and are not the primary mechanism for transporting

water to the shelf slope. As a result, DW is first advected by the mean flow to the main canyons (Barrow, Central, and Herald), flows down the canyons in intermittent bursts, and finally is transported into the interior of the Canada Basin by eddies. Maximum salinity on the shelf is more consistent with values obtained by Winsor and Chapman (2002) using high-resolution meteorological forcing than using NCEP atmospheric forcing. Overall, $4191 \pm 1152 \text{ km}^3 \text{ yr}^{-1}$ to $4863 \pm 1440 \text{ km}^3 \text{ yr}^{-1}$ of DW in the density anomaly range σ of 26.0–27.5 kg m^{-3} flows across gates BC and CC + HC (Fig. 11a). Seaward of the shelf break, at depths of 50–150 m, eddies transport 60%–90% of the DW into the Arctic interior. There is, however, a pronounced drift in eddy transport contribution, which we speculate is related to the drift of core Atlantic Water temperature in the model. Further investigation, which is beyond the scope of this study, is

required to fully understand the temperature drift due to resolution increase and the eddy transport drift.

4) COMPARISON OF PRODUCTION RATES

Here, we compare UHW production rates obtained from the CM94 procedure [section 3a(2)] and from the model simulations [section 3b(2)]. The mean annual rates are $5740 \pm 1420 \text{ km}^3 \text{ yr}^{-1}$ for the CM94 procedure (Table 2) and $4191 \pm 1152 \text{ km}^3 \text{ yr}^{-1}$ to $4863 \pm 1440 \text{ km}^3 \text{ yr}^{-1}$ for the 9- and 4-km model solutions (Fig. 11a). Although the estimates are of the same order, their corresponding annual time series have very low correlation (<0.1 , correlation between Fig. 5b and the combined Figs. 10c,e).

Between the two model solutions, the main difference is a 25% higher flux of DW down Barrow Canyon in the 4-km solution compared to 9-km solution. This difference amounts to $\sim 570 \text{ km}^3 \text{ yr}^{-1}$ and is about half of the interannual variability. One possible explanation is that Barrow Canyon is better resolved in the 4-km bathymetry. DW flux down CC + HC only differs by 4% ($\sim 100 \text{ km}^3 \text{ yr}^{-1}$) between the two solutions; this difference is negligible compared to the interannual variability ($640\text{--}790 \text{ km}^3 \text{ yr}^{-1}$).

Within the uncertainty and interannual variability ranges, the net annual UHW production rates are similar to previous estimates of $6310 \text{ km}^3 \text{ yr}^{-1}$ from a 1958–97 numerical model study (Winsor and Björk 2000) and of $6370 \pm 3150 \text{ km}^3 \text{ yr}^{-1}$ from an idealized box model inversion constrained by mass, heat, salt, and $\delta^{18}\text{O}$ measurements (Goldner 1999). CM94 reports an annual DW production of $8430\text{--}11\,650 \text{ km}^3$ (Table 2, last column) and can be compared to our estimate of $7450 \pm 1100 \text{ km}^3$ (including $\Delta\sigma_1$ contribution; fourth column in Table 2). These rates are likely overestimations due to assumption 5 in their method. Their corresponding UHW production rate is expected to be lower than that of DW.

Based on the UHW annual rate obtained in this study and assuming a Canada Basin area of $\sim 10^6 \text{ km}^2$ and a UHW thickness of 50–100 m, the ventilation rate is 10–21 yr. This rate is comparable to the ventilation period of 10–20 yr suggested by Pickart et al. (2005) based on his estimated production rates of $9500 \text{ km}^3 \text{ yr}^{-1}$ for dense water and $2525\text{--}5050 \text{ km}^3 \text{ yr}^{-1}$ for upper halocline water. We caution again that the rates reported here can be sensitive to the atmospheric boundary conditions used in the model, as shown in Winsor and Chapman (2002).

4. Summary

We use two regional, coupled ocean and sea ice simulations to study the source and pathway of dense water

(DW) and upper halocline water (UHW) in the western Arctic Ocean. The first simulation has 9-km horizontal grid spacing, typical of resolutions used for pan-Arctic Ocean studies. The second simulation has 4-km horizontal grid spacing, hence admitting eddies and providing insight on the role of resolution in representing DW and UHW formation and transport.

The two simulations are first evaluated using satellite-derived estimates of sea ice production (Fig. 5a). Overall, the simulations overestimate the mean ice production by $13 \text{ km}^3 \text{ yr}^{-1}$ and underestimate ice production variability in the Chukchi Sea between Point Barrow and Cape Lisburne, a result that is likely governed by JRA25, the atmospheric forcing used here. A high correlation of 0.90 between simulated and satellite-derived ice production, however, indicates that the model can produce realistic polynyas next to the coast of Alaska during winter months. The 17-yr model solutions show that DW forms in the Chukchi and Bering Seas as a result of polynyas and of sea ice growth during the winter (Figs. 6–9).

Two methods were used to calculate DW and UHW productions and transports. The first method is based on sea ice productions using satellite ice concentration, following the CM94 procedure. This method yields a net UHW production of $5740 \pm 1420 \text{ km}^3 \text{ yr}^{-1}$ (Fig. 5b).

The second method is based on the 9- and 4-km model $T\text{--}S$ and velocity fields. This method yields a net UHW production of $4190\text{--}4860 \pm 1440 \text{ km}^3 \text{ yr}^{-1}$ (Figs. 10, 11a). The largest contribution to the difference in DW transport between the 9- and 4-km simulations is the $\sim 25\%$ higher flux down Barrow Canyon in the 4-km simulation. This difference, however, is about half the interannual variability of flux down Barrow Canyon. Thus, within the uncertainty and variability range, UHW production rates in the 9- and 4-km simulations are comparable.

UHW production rates obtained in this study can also be compared with published estimates that range between 6310 and $11\,650 \text{ km}^3 \text{ yr}^{-1}$ (Table 2; CM94; Winsor and Björk 2000; Goldner 1999). Based on the rates obtained in this study, UHW ventilation time is 10–21 yr. For comparison, Pickart et al. (2005) estimated it takes 10–20 yr to ventilate the upper halocline based on their off-shelf DW flow estimate of $\sim 9500 \text{ km}^3 \text{ yr}^{-1}$. We caution that the rates reported here can be sensitive to the atmospheric boundary conditions used by the model, as shown in Winsor and Chapman (2002).

Passive tracers released in the 9-km simulation are used to study the geographic dependency of DW flows. These passive tracers show that water with the highest density ($\sigma > 27 \text{ kg m}^{-3}$) is produced in the Gulf of Anadyr and along the east Siberian coast immediately north of Bering Strait (regions C and G; Fig. 11b) and

that it reaches the Arctic interior by flowing down Central and Herald Canyons (Figs. 10d, 11b). Within the uncertainties and interannual variability, approximately the same volume of DW flows down Barrow Canyon and down the combined Central and Herald Canyons (Fig. 11a) before feeding the upper halocline.

The 4-km simulation permits investigation of eddy transports on the Chukchi Shelf and in the Canada Basin interior. At depths of 50–150 m, UHW is transported from the shelf break along Barrow Canyon into the Canada Basin interior by eddies with typical diameter of ~30 km (Fig. 13). The contribution of eddies to the total transport at these depths is 60%–70% between 1994 and 2002 and higher after 2003. We note that there is a drift in eddy transport contribution, which would require further investigation to fully understand. The generally high contribution of eddy transport at these depths agrees with results from Spall et al. (2008).

On the Chukchi Shelf, a small number of eddies is generated in the vicinity of brine-enriched DW that forms during the winter as a result of sea ice formation (Fig. 6e). The growth rate of ~6 days and the ~30-km diameter of these eddies are consistent with the theoretical calculations of GC95 and CG95. These eddies, however, lose their coherent structures a short distance from the source and are not the primary agent for DW transport to the shelf slope in the model. A mean along-shelf flow with speed of 0.05–0.1 m s⁻¹, which is 5–10 times the predicted mean eddy speed of 0.01–0.02 m s⁻¹ (GC95), advects DW downstream from the source into the canyons. We speculate that this strong mean flow on the shelf, along with bathymetric variations, potentially contribute to the small eddy growth and to negligible eddy transport on the shelf.

Intermittent flows of DW down Barrow Canyon begin in February and then down Central and Herald Canyons begin in April (Figs. 10a,b). The results obtained here are consistent with mooring observations (Danielson et al. 2006) and with results from primitive equation numerical model (Chapman 2000), which show (i) negligible eddy energy associated with polynyas in the St. Lawrence Island region, (ii) DW being advected along-shore away from the source by the mean flow, and (iii) downstream eddy development and eddy-associated intermittent flows that transport DW down the canyons.

The contribution of eddies to the transport of DW on the Chukchi Shelf thus remains an open question. The 4-km solution is likely too coarse to fully resolve eddies on the shelf, and the studies of GC95 and CG95 are too idealized to realistically represent the formation and dissipation of these eddies. A valuable future study would be to compare results of the 9- and 4-km solutions with a yet higher-resolution solution that can resolve

realistic eddy–bathymetry–current interactions on the shelf. Initial frontal instability that results in the formation of these eddies scale with the baroclinic Rossby radius, which is estimated to be 4–8 km on the shallow Chukchi Shelf (GC95; Chapman and Gawarkiewicz 1997). When the forcing region has a length scale larger than the Rossby radius, GC95 and Chapman and Gawarkiewicz (1997) showed that the eventual eddies scale with the forcing region width but remain within the range of 20–30 km. The relevant question is then at what higher resolution we should expect to resolve the frontal instability and eddies. GC95 showed in one of their idealized simulations that a 2-km horizontal grid spacing can resolve eddies on the shelf and that higher horizontal resolution (finer grid spacing) yielded only minor differences. This same conclusion was also reached by Chapman and Gawarkiewicz (1997). On a related note, GC95 and Chapman and Gawarkiewicz (1997) showed that at high latitude, when the shelf is very shallow such that rotational effect is not important, DW sinks quickly to the bottom of the ~50-m shelf. Cross sections of their respective results showed that the bottom-trapped DW can have thickness of 20–50 m (see also Fig. 11 in CG95). Thus, we believe grid spacings of 10 m in the vertical direction and ~2 km in the horizontal direction should be used in future studies to sufficiently address the contribution of shelf eddies to DW and UHW ventilation.

The conclusion of this study, however, consistent with the observational and numerical results of Danielson et al. (2006) and Chapman (2000), is that eddies have a negligible contribution to transport of DW on the shelf.

Acknowledgments. This work is funded by the ECCO2 project, a contribution to the NASA Modeling Analysis and Prediction (MAP) program, and by Grant NSF ARC-1023499. We gratefully acknowledge computational resources and support from the NASA Advanced Supercomputing (NAS) Division and from the JPL Supercomputing and Visualization Facility (SVF). The research described in this paper was partially carried out at the Jet Propulsion Laboratory, California Institute of Technology, under a contract with NASA. We thank R. Woodgate for providing data of fluxes across Bering Strait and for helpful discussion and R. Pickart and V. A. Wilken-Jon and I. Fenty for discussion of hydrographic profiles and eddy transport in the Chukchi Sea. Finally, we thank two anonymous reviewers for valuable comments.

REFERENCES

- Aagaard, K., L. Coachman, and E. Carmack, 1981: On the halocline of the Arctic Ocean. *Deep-Sea Res.*, **28A** (6), 529–545.

- Antonov, J. I., R. A. Locarnini, T. P. Boyer, A. V. Mishonov, and H. E. Garcia, 2006: *Salinity*. Vol. 2, *World Ocean Atlas 2005*, NOAA Atlas NESDIS 62, 182 pp.
- Cavaliere, D., and S. Martin, 1994: The contribution of Alaskan, Siberian, and Canadian coastal polynyas to the cold halocline layer of the Arctic Ocean. *J. Geophys. Res.*, **99** (C9), 18 343–18 362.
- Chapman, D., 2000: The influence of an alongshelf current on the formation and offshore transport of dense water from a coastal polynya. *J. Geophys. Res.*, **105**, 24 007–24 019.
- , and G. Gawarkiewicz, 1995: Offshore transport of dense shelf water in the presence of a submarine canyon. *J. Geophys. Res.*, **100** (C7), 13 373–13 387.
- , and —, 1997: Shallow convection and buoyancy equilibration in an idealized coastal polynya. *J. Phys. Oceanogr.*, **27**, 555–566.
- Danielson, S., K. Aagaard, T. Weingartner, S. Martin, P. Winsor, G. Gawarkiewicz, and D. Quadfasel, 2006: The St. Lawrence polynya and the Bering shelf circulation: New observations and a model comparison. *J. Geophys. Res.*, **111**, C09023, doi:10.1029/2005JC003268.
- Gawarkiewicz, G., 2000: Effects of ambient stratification and shelfbreak topography on offshore transport of dense water on continental shelves. *J. Geophys. Res.*, **105** (C2), 3307–3324.
- , and D. Chapman, 1995: A numerical study of dense water formation and transport on a shallow, sloping continental shelf. *J. Geophys. Res.*, **100** (C3), 4489–4507.
- Goldner, D., 1999: Steady models of Arctic shelf-basin exchange. *J. Geophys. Res.*, **104**, 29 733–29 755.
- Heimbach, P., D. Menemenlis, M. Losch, J.-M. Campin, and C. Hill, 2010: On the formulation of sea-ice models. Part 2: Lessons from multi-year adjoint sea ice export sensitivities through the Canadian Arctic Archipelago. *Ocean Modell.*, **33**, 145–158.
- Holloway, G., A. Nguyen, and Z. Wang, 2011: Oceans and ocean models as seen by current meters. *J. Geophys. Res.*, **116**, C00D08, doi:10.1029/2011JC007044.
- Jakobsson, M., R. Macnab, L. Mayer, R. Anderson, M. Edwards, J. Hatzky, H. W. Schenke, and P. Johnson, 2008: An improved bathymetric portrayal of the Arctic Ocean: Implications for ocean modeling and geological, geophysical and oceanographic analyses. *Geophys. Res. Lett.*, **35**, L07602, doi:10.1029/2008GL033520.
- Lammers, R., A. Shiklomanov, C. Vorosmarty, B. Fekete, and B. Peterson, 2001: Assessment of contemporary Arctic river runoff based on observational discharge records. *J. Geophys. Res.*, **106** (D4), 3321–3334.
- Locarnini, R. A., A. V. Mishonov, J. I. Antonov, T. P. Boyer, and H. E. Garcia, 2006: *Temperature*. Vol. 1, *World Ocean Atlas 2005*, NOAA Atlas NESDIS 62, 182 pp.
- Losch, M., D. Menemenlis, P. Heimbach, J.-M. Campin, and C. Hill, 2010: On the formulation of sea-ice models. Part 1: Effects of different solver implementations and parameterizations. *Ocean Modell.*, **33**, 129–144.
- Marks, K. M., and W. H. F. Smith, 2006: An evaluation of publicly available global bathymetry grids. *Mar. Geophys. Res.*, **27**, 19–34.
- Marshall, J., A. Adcroft, C. Hill, L. Perelman, and C. Heisey, 1997a: A finite-volume, incompressible Navier-Stokes model for studies of the ocean on parallel computers. *J. Geophys. Res.*, **102** (C3), 5753–5766.
- , C. Hill, L. Perelman, and A. Adcroft, 1997b: Hydrostatic, quasi-hydrostatic and non-hydrostatic ocean modeling. *J. Geophys. Res.*, **102** (C3), 5733–5752.
- Martin, S., R. Drucker, R. Kwok, and B. Holt, 2004: Estimation of the thin ice thickness and heat flux for the Chukchi Sea Alaskan coast polynya from Special Sensor Microwave/Imager data, 1990–2001. *J. Geophys. Res.*, **109**, C10012, doi:10.1029/2004JC002428.
- , —, —, and —, 2005: Improvements in the estimates of ice thickness and production in the Chukchi Sea polynyas derived from AMSR-E. *Geophys. Res. Lett.*, **32**, L05505, doi:10.1029/2004GL022013.
- Melling, H., 1993: The formation of a haline shelf front in wintertime in an ice-covered Arctic sea. *Cont. Shelf Res.*, **13**, 1123–1147.
- Menemenlis, D., I. Fukumori, and T. Lee, 2005a: Using Green's functions to calibrate an ocean general circulation model. *Mon. Wea. Rev.*, **133**, 1224–1240.
- , and Coauthors, 2005b: NASA supercomputer improves prospects for ocean climate research. *Eos, Trans. Amer. Geophys. Union*, **86**, 89, doi:10.1029/2005EO090002.
- , J. Campin, P. Heimbach, C. Hill, T. Lee, A. Nguyen, M. Schodlock, and H. Zhang, 2008: Ecco2: High resolution global ocean and sea ice data synthesis. *Mercator Ocean Quarterly Newsletter*, No. 31, Mercator Ocean, Ramonville-Saint-Agne, France, 13–21.
- Nguyen, A. T., D. Menemenlis, and R. Kwok, 2009: Improved modeling of the Arctic halocline with a subgrid-scale brine rejection parameterization. *J. Geophys. Res.*, **114**, C11014, doi:10.1029/2008JC005121.
- , —, and —, 2011: Arctic ice-ocean simulation with optimized model parameters: Approach and assessment. *J. Geophys. Res.*, **116**, C04025, doi:10.1029/2010JC006573.
- Oke, P. R., and Coauthors, 2002: A modeling study of the three-dimensional continental shelf circulation off Oregon. Part I: Model–data comparisons. *J. Phys. Oceanogr.*, **32**, 1360–1382.
- Onogi, K., and Coauthors, 2007: The JRA-25 reanalysis. *J. Meteor. Soc. Japan*, **85**, 369–432.
- Pickart, R. S., 2004: Shelfbreak circulation in the Alaskan Beaufort Sea: Mean structure and variability. *J. Geophys. Res.*, **109**, C04024, doi:10.1029/2003JC001912.
- , T. J. Weingartner, L. J. Pratt, S. Zimmermann, and D. J. Torres, 2005: Flow of winter-transformed Pacific water into the western Arctic. *Deep-Sea Res. II*, **52**, 3175–3198.
- Rudels, B., E. Jones, U. Schauer, and P. Eriksson, 2004: Atlantic sources of the Arctic Ocean surface and halocline waters. *Polar Res.*, **23**, 181–208.
- Shimada, K., M. Itoh, S. Nishimo, F. McLaughlin, E. Carmack, and A. Proshutinsky, 2005: Halocline structure in the Canada Basin of the Arctic Ocean. *Geophys. Res. Lett.*, **32**, L03605, doi:10.1029/2004GL021358.
- Spall, M. A., R. S. Pickart, P. S. Frantantoni, and A. J. Plueddemann, 2008: Western Arctic shelfbreak eddies: Formation and transport. *J. Phys. Oceanogr.*, **38**, 1644–1668.
- Steele, M., and T. Boyd, 1998: Retreat of the cold halocline layer in the Arctic Ocean. *J. Geophys. Res.*, **103** (C5), 10 419–10 435.
- Tomczak, M., 1981: A multi-parameter extension of temperature/salinity diagram techniques for the analysis of non-isopycnal mixing. *Prog. Oceanogr.*, **10**, 147–171.
- Wang, Z., G. Holloway, and C. Hannah, 2011: Effects of parameterized eddy stress on volume, heat, and freshwater transports through Fram Strait. *J. Geophys. Res.*, **116**, C00D09, doi:10.1029/2010JC006871.
- Weingartner, T., D. Cavaliere, K. Aagaard, and Y. Sasaki, 1998: Circulation, dense water formation, and outflow on the northeast Chukchi shelf. *J. Geophys. Res.*, **103** (C4), 7647–7661.

- Winsor, P., and G. Björk, 2000: Polynya activity in the Arctic Ocean from 1958 to 1997. *J. Geophys. Res.*, **105**, 8789–8803.
- , and D. C. Chapman, 2002: Distribution and interannual variability of dense water production from coastal polynyas on the Chukchi Shelf. *J. Geophys. Res.*, **107**, 3079, doi:10.1029/2001JC000984.
- Woodgate, R. A., and K. Aagaard, 2005: Revising the Bering Strait freshwater flux into the Arctic Ocean. *Geophys. Res. Lett.*, **32**, L02602, doi:10.1029/2004GL021747.
- , —, J. Swift, K. K. Falkner, and W. M. Smethie Jr., 2005a: Pacific ventilation of the Arctic Ocean's lower halocline by upwelling and diapycnal mixing over the continental margin. *Geophys. Res. Lett.*, **32**, L18609, doi:10.1029/2005GL023999.
- , —, and T. J. Weingartner, 2005b: Monthly temperature, salinity, and transport variability of the Bering Strait through flow. *Geophys. Res. Lett.*, **32**, L04601, doi:10.1029/2004GL021880.
- , T. Weingartner, and R. Lindsay, 2010: The 2007 Bering Strait oceanic heat flux and anomalous Arctic sea-ice retreat. *Geophys. Res. Lett.*, **37**, L01602, doi:10.1029/2009GL041621.
- Zhang, J., and D. Rothrock, 2003: Modeling global sea ice with a thickness and enthalpy distribution model in generalized curvilinear coordinates. *Mon. Wea. Rev.*, **131**, 681–697.